

Grounding the Ungrounded: A Spectral-Graph Framework for Quantifying Hallucinations in multimodal LLMs

Supratik Sarkar^{*1} and Swagatam Das^{†2}

¹Morgan Stanley

²Indian Statistical Institute (Kolkata), India

October 6, 2025

Abstract

Hallucinations in LLMs—especially in multimodal settings—undermine reliability. We present a rigorous, information-geometric framework in diffusion dynamics that quantifies hallucination in MLLMs: model outputs are embedded spectrally on multimodal graph Laplacians, and gaps to a truth manifold define a semantic-distortion metric. We derive Courant–Fischer bounds on a temperature-dependent hallucination energy and use RKHS eigenmodes to obtain modality-aware, interpretable measures that track evolution over prompts and time. This reframes hallucination as measurable and bounded, providing a principled basis for evaluation and mitigation.

1 Introduction

Large language models (LLMs) and their multimodal variants (MLLMs) are powerful generators, but reliability or truthfulness remains a core limitation. A central drawback is the hallucinated content that is ungrounded or inconsistent with inputs - which is unacceptable and significantly risky in medicine, law, and finance [1–3]. Prior work offers taxonomies, datasets, and benchmarks for analysis and evaluation [1, 2, 4], and recent multimodal studies emphasize empirical detection/mitigation [5]; however, most approaches rely on heuristics, proxy metrics, or human annotation rather than principled quantification.

On the theory side, complementary work include token-level analysis of hallucinated predictions [6], Bayesian sequential detection [7], entropy-style uncertainty probes [8], latent-space steering to separate truthful vs. hallucinated generations [9], and reference-free ranking for multimodal hallucinations [10]. Emerging spectral/graph perspectives probe representations and attention, but are largely detection-oriented and unimodal [11].

Gap. The field currently lacks a quantitative, theory-backed, modality-aware framework that treats hallucination as a measurable quantity (with temporal dynamics and guarantees), rather than only a classification/detection outcome.

Our contribution. We introduce a spectral-graph framework that makes hallucination in MLLMs measurable and bounded in the context of time-indexed temperature profiles:

- (a) We model the grounding across modalities via optimal-transport paths in diffusion dynamics and embed them in RKHS, yielding a structural view of semantic consistency.
- (b) We represent outputs on multimodal graph Laplacians and derive tight Courant–Fischer (CF) bounds on hallucination heatmap as a function of time-indexed temperature.

^{*}supratik.sarkar@morganstanley.com

[†]swagatam.das@isical.ac.in

(c) *Empirical validation*: Across nine 3D panels (COCO/VQAv2/AudioCaps \times CLIP+Whisper+T5, BLIP+CLIP+Whisper, SigLIP+Whisper+T5), $\mathcal{E}_{\text{hall}}^{\text{multi}}$ lies between panel-specific CF planes with a strictly positive lower envelope that tightens at lower temperature (and higher diffusion); full $\varepsilon/\tau/h/\rho$ ablations and runtimes in the supplement.

This shifts hallucination study from qualitative detection to quantitative, modality-aware, and interpretable analysis. To our knowledge, it is the first attempt to provide spectral bounds on hallucination for MLLMs followed by a time-indexed temperature annealing, offering a principled basis for evaluation and potential mitigation.

2 Related Work

Kalai & Vempala show that, for calibrated LMs, the hallucination rate is lower-bounded by a Good–Turing-style “monofact” mass - establishing an inherent trade-off between calibration and truthfulness [12]; while their recent work generalizes this via an IIV reduction that ties generative errors to binary-classification - advocating IDK-tolerant evaluation [13]. Empirical study of LM hallucinations spans mechanistic probes that surface interpretable features for diagnosis [14], retrieval-grounded detection and evaluation [15, 16], broad benchmark suites like HalluEval [17], Hallu-PI [4], GraphEval [18], and early vision–language analyses of object hallucination [19]. Comprehensive surveys catalog causes, detection, and mitigation strategies [1, 20].

Recent work exploits uncertainty and structural signals: semantic-entropy probes [8], Bayesian sequential estimation [7], token-level dynamics of hallucinated predictions [6], zero-shot reasoning signals [21], and sampling-based self-consistency checks (SelfCheckGPT) [22]. Graph/spectral methods flag hallucinations via KG self-checks (FactSelfCheck) [23], attention Laplacian eigen-spectra (LapEigvals) [24], and topological cues on hallucination graphs [25].

3 Preliminaries

We begin by establishing the mathematical foundations of our framework. MLLM outputs are embedded as nodes on a knowledge graph Laplacian, and grounding gaps along this graph collectively define a quantifiable hallucination metric. Figure 1 sketches our approach.

3.1 Mathematical Foundations

Let \mathcal{X} denote the measurable^{A.1}¹ set of all possible model outputs of a multimodal LLM, with $\mathcal{F}_{\mathcal{X}}$ being the σ -algebra over \mathcal{X} and μ being the base measure [26]; e.g., the count measure for discrete outputs like token sequence or the Lebesgue measure for continuous outputs like embeddings [27]. We assume \mathcal{X} is continuously embedded in a separable Reproducing Kernel Hilbert space (RKHS) denoted by $(\mathcal{H}, \langle \cdot, \cdot \rangle_{\mathcal{H}})$ which is associated with a positive-definite kernel,

$$K : \mathcal{X} \times \mathcal{X} \rightarrow \mathbb{R}^+. \quad (1)$$

The kernel $K(x_1, x_2)$ encodes the semantic relationships between two distinct points or outputs x_1 and $x_2 \forall (x_1 \neq x_2) \in \mathcal{X}$; for example, through embedding-based or ontology-aware distance measures, or co-reference resolution. For a product kernel in an MLLM, refer to Eq. (7) later.

Within this $(\mathcal{X}, \mathcal{F}_{\mathcal{X}}, \mu)$ space, there exist two kinds of “truth” (the idea imported from [12]):

- (i) The semantic factoid space \mathcal{K} which encompasses all semantically valid and coherent outputs that include empirically plausible facts, contextually appropriate completions, and domain-consistent inferences aligned with the prompt and background knowledge - importantly, elements of \mathcal{K} need not be verifiable, but they remain semantically valid within the modeled domain.

¹Footnotes are added in chronological order and collected in Appendix A.

- (ii) The semantic ground-truth manifold \mathcal{K}_g , as a stricter subregion of \mathcal{K} , which consists of outputs only verifiably correct or true facts that include factual assertions supported by empirical evidence or directly observed information — elements of \mathcal{K}_g can be properly referred to as grounded in reality.

Thus the semantic plausibility/ground-truth nesting and, for a given prompt $p \in \mathcal{P}$, the hallucination criterion for each output denoted by $x \in \mathcal{X}$ are:

$$\mathcal{K}_g \subseteq \mathcal{K} \subset \mathcal{X}, \quad x \in \mathcal{X} \setminus \mathcal{K}. \quad (2)$$

Note: $x \in \mathcal{K} \setminus \mathcal{K}_g$ is a non-grounded output, but still semantically plausible and strictly not hallucination.

3.2 Modeling the LLM outputs

We begin with the baseline assumptions:

Assumption 1 (General output distribution). *The LLM outputs can be characterized by a conditional probability distribution $f_p(x)$ that denotes the likelihood of generating output x given a prompt p :*

$$f_p : \mathcal{X} \rightarrow [0, \infty), \quad f_p \in L^1(\mathcal{X}, \mathcal{F}_{\mathcal{X}}, \mu) \cap \mathcal{H}, \quad x \mapsto f_p(x), \quad (3)$$

which ensure $\int_X f_p(x) d\mu(x) = 1$.

Let $f_p^{\mathcal{K}}$ denote the restricted distribution on the semantic plausibility space \mathcal{K} :

$$f_p^{\mathcal{K}}(x) := \frac{\mathbf{1}_{\{x \in \mathcal{K}\}} f_p(x)}{\int_{\mathcal{K}} f_p(x') d\mu(x')} \equiv \frac{\mathbf{1}_{\{x \in \mathcal{K}\}} f_p(x)}{\mathbb{P}_{f_p}(\mathcal{K})}, \quad \text{where, } \mathbf{1}_{\{x \in \mathcal{K}\}} = \begin{cases} 1 & \text{if } x \in \mathcal{K}, \\ 0 & \text{otherwise.} \end{cases} \quad (4)$$

Here, $\int_{\mathcal{K}} f_p(x') d\mu(x') = \mathbb{P}_{f_p}(\mathcal{K})$ is a normalization constant in the restricted distribution.

Assumption 2 (Ground-truth generative distribution). *In line with Assumption 1, g denotes the reference distribution on the ground-truth manifold \mathcal{K}_g . Unlike f_p or f_p^K , g is the gold reference which is not model-induced and hence, may not share support with f_p except inside \mathcal{K}_g and it is truly independent of prompts in the generative sense (but conditioned on the same prompt contextually).*

Thus, we do not assume any parametric form for the ground-truth distribution g and rather treat it as an abstract measure over \mathcal{K}_g :

$$\text{supp}(g) \subseteq \mathcal{K}_g, \quad g : \mathcal{K}_g \rightarrow [0, \infty), \quad g \in L^1(\mathcal{K}_g, \mathcal{F}_{\mathcal{X}}|_{\mathcal{K}_g}, \mu'). \quad (5)$$

Eq. (5) ensures $\int_{\mathcal{K}_g} g(x) d\mu'(x) = 1$ with notations used in consistency with Eq. (3) and μ' playing the same role of μ , but not necessarily equal to μ . See comments^{A.2} in Appendix A.

4 Theoretical Analysis

In this section, we present a theoretical framework that couples a smoothed information-geometric score derived from the Kullback–Leibler (KL) paradigm^{A.3} with a multimodal energy formulation to quantify and track hallucinations in MLLMs.

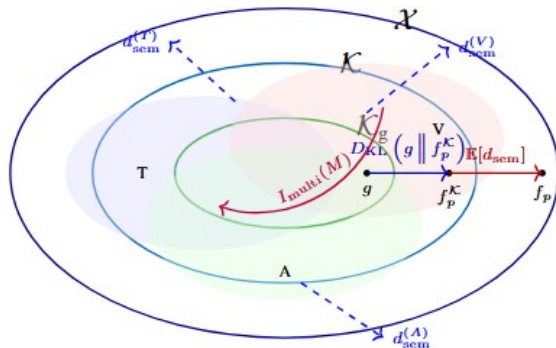


Figure 1: Multimodal nested-manifold view of hallucinations. Hollow ellipses denote \mathcal{X} , \mathcal{K} , \mathcal{K}_q .

4.1 Semantic Distortion

We establish the following theorem followed by stating a remark to set the stepping stone.

Theorem 1 (KL-calibrated smoothed score for hallucination). *Let a smoothing mass $\varepsilon \in (0, 1)$ and a baseline density be fixed, with finite $\rho(x) > 0$ μ -a.e. and $\int_{\mathcal{X}} \rho(x) d\mu(x) = 1$; let $K_h(\cdot, \cdot) \in (0, \infty)$ be a μ -Markov kernel (bandwidth $h > 0$) and $T_h : L^1(\mu) \rightarrow L^1(\mu)$ be a linear smoother defined for $q : \mathcal{X} \rightarrow \mathbb{R}$ by $(T_h q)(x_1) := \int_{\mathcal{X}} K_h(x_1, x_2) q(x_2) d\mu(x_2)$; let the ε -smoothed model be $\tilde{f}_{p, \varepsilon}(x) := (1 - \varepsilon)f_p(x) + \varepsilon\rho(x)$ with its \mathcal{K} -restricted renormalization $\tilde{f}_{p, \varepsilon}^{\mathcal{K}}(x_2) := \mathbf{1}_{\{x_2 \in \mathcal{K}\}} \tilde{f}_{p, \varepsilon}(x_2) / \int_{\mathcal{K}} \tilde{f}_{p, \varepsilon}(x) d\mu(x)$; and let a measurable selector $\Pi_{\mathcal{K}} : \mathcal{X} \rightarrow \mathcal{K}$ satisfy $\Pi_{\mathcal{K}}(x) = x$ ($\forall x \in \mathcal{K}$) or nearest point with convexity in \mathcal{K} (otherwise). Then the semantic distortion*

$$d_{\text{sem}}^{(\varepsilon, h)}(x; \mathcal{K}, \mathcal{X}) := \left[\log((T_h \tilde{f}_{p, \varepsilon}^{\mathcal{K}})(\Pi_{\mathcal{K}}(x))) - \log((T_h \tilde{f}_{p, \varepsilon})(x)) \right]_+, \quad (6)$$

serves as a KL-calibrated smoothed pointwise information gap for tracking hallucinations across prompts and remains as a reference-free (independent-of- g) statistic in language models.

Proof sketch: Strict positivity from $\tilde{f}_{p, \varepsilon} = (1 - \varepsilon)f_p + \varepsilon\rho$ and Markov K_h makes both smoothed terms > 0 , so Eq. (6) is finite. If $x \in \mathcal{K}$, $\Pi_{\mathcal{K}}(x) = x$ and the \mathcal{K} -restricted smoother $>$ the unconditional smoother at x ; if $x \notin \mathcal{K}$, smoothing at $\Pi_{\mathcal{K}}(x) \in \mathcal{K}$ dominates the mixed mass at x . Detailed proof is found in Appendix B.1. \square

Remark 1. The score in Eq. (6) is g -agnostic and thus usable when g is unobservable^{A.4} or partially verified in various real-world scenarios. In practice, we set a small smoothing mass $\varepsilon \in [10^{-6}, 10^{-2}]$, choose h by validation, take K_h as a positive row-normalized kernel over embeddings/tokens, and we implement $\Pi_{\mathcal{K}}$ as a measurable nearest-neighbour selector on a finite reference set from \mathcal{K} .

4.2 Extension to Multi-modal Grounding

The intuition behind this setting of multimodality is: in image-grounded or dialogue models, semantic grounding depends on multiple modalities — e.g., text, image or video, dialog or audio-history etc. and the RKHS is then extended to a multi-modal product kernel space. In multi-modal settings, where the LLM outputs involve textual (T), visual (V), audio (A) modalities, we define a joint output space (\mathcal{X}) embedded into a composite RKHS (\mathcal{H}) equipped with a product kernel (K) between two distinct points (i.e., outputs) $\forall(x_1 \neq x_2) \in \mathcal{X}$ as

$$\mathcal{X} : \times_M \mathcal{X}_M, \quad x = (x^{(M)})_{x^{(M)} \in \mathcal{X}_M}, \quad \mathcal{H} := \bigotimes_M \mathcal{H}_M, \quad K(x_1, x_2) = \prod_M K_M(x_1^{(M)}, x_2^{(M)}), \quad (7)$$

pertaining to each modality $\forall M \in \mathcal{M} := \{T, V, A\}$, where the prompts can also be categorized into a composite prompt space $\mathcal{P} : \times_M \mathcal{P}_M$, with each prompt $p = (p^{(M)})_{p^{(M)} \in \mathcal{P}_M}$ in a modality-aware prescription to accommodate three different kinds of probable inputs (i.e., T, V & A) for the sake of completeness. However, in the following calculation in this paper, we restrict ourselves only to the notion of p without any loss of generality. Expanded form^{A.5} of Eq. (7) is found in Appendix A.

4.3 Formulations to hallucination Energy

To begin with, we are after a fruitful formulation of $f_p(x)$ that connects the model output distribution to an underlying energy landscape to enable modal interpretability, temperature-driven exploration, and spectral graph analysis. The total energy functional $\mathcal{E}(x, p, \cdot) : \mathcal{X} \times \mathcal{P} \rightarrow \mathbb{R}^+$ associated with the model input-output plus suppressed parameters can be decomposed into intra-modal, pairwise cross-modal, and joint multimodal interactions. This decomposition allows us to localize the sources of hallucination within and across modalities.

Assumption 3 (Hallucination energy functional in MLLMs). *The modality-aware decomposition reads as:*

$$\mathcal{E}(x, p, \cdot) = \sum_{M \in \mathcal{M}} \mathcal{E}_M(x^{(M)}, p, \cdot) + \sum_{\substack{M, M' \in \mathcal{M} \\ M \neq M'}} \mathcal{E}_{MM'}(x^{(M)}, x^{(M')}, p, \cdot) + \mathcal{E}_{\mathcal{M}}(x, p, \cdot). \quad (8)$$

Refer to Section 5.1 for the similar construction in terms of multimodal Laplacians. See term-wise explanations^{A.6} in Appendix A.

Assumption 4 (Feature maps for boundedness). *Using the results of Moore–Aronszajn theorem [28], for a positive definite kernel K_M in a measurable output space $(\mathcal{X}, \mathcal{F}_{\mathcal{X}}, \mu)$ aligned with Section 3.1, let $\Phi_M : \mathcal{X}_M \rightarrow \mathcal{H}_M$ be its feature map treated as infinite-dimensional linear operator for each modality $M \in \mathcal{M}$ under the constraint of boundedness: $\sup_{x^{(M)} \in \mathcal{X}_M} \|\Phi_M(x^{(M)})\|_{\mathcal{H}_M} < \infty$. (See explicit justification^{A.7} in Appendix A.)*

For each modality M , the (fixed) embedding pipeline with an implicit kernel^{A.8} in a higher-dimensional RKHS induces $\Phi_M : \mathcal{X}_M \rightarrow \mathcal{H}_M$ such that $\langle \Phi_M(x_1), \Phi_M(x_2) \rangle_{\mathcal{H}_M} = K_M(x_1, x_2)$.

Assumption 5 (Prompt embeddings). *Let $(\mathcal{P}, \mathcal{F}_{\mathcal{P}}, \nu)$ be a measurable space on prompts with ν being finite. For each modality $M \in \mathcal{M}$, the prompt embedding $\Psi_M : \mathcal{P} \rightarrow \mathcal{H}_M$ satisfies boundedness: $\sup_{p \in \mathcal{P}} \|\Psi_M(p)\|_{\mathcal{H}_M} < \infty$ and stability: Ψ_M is continuous (equivalently, Lipschitz with finite constant $\text{Lip}(\Psi_M)$) in the chosen topology/metric on \mathcal{P} . (See explicit justification^{A.7} in Appendix A.)*

Assumption 6 (Output distribution in Boltzman form). *We view $f_p(x)$ as a normalized surrogate over candidate outputs or latent representations with respect to a finite (or bounded) base measure μ . Under bounded embeddings and compact support (or bounded energy), the partition function $Z(p, \mathcal{T}_t)$ is finite, making Eq. (9) well-defined. (See explicit justification^{A.9} in Appendix A.)*

Lemma 1 (Joint measurability of cross inner products). *If $\Phi_M : (\mathcal{X}_M, \mathcal{F}_{\mathcal{X}_M}) \rightarrow (\mathcal{H}_M, \mathcal{B}(\mathcal{H}_M))$ and $\Psi_M : (\mathcal{P}, \mathcal{F}_{\mathcal{P}}) \rightarrow (\mathcal{H}_M, \mathcal{B}(\mathcal{H}_M))$ are Bochner measurable into a separable Hilbert space \mathcal{H}_M where $\mathcal{B}(\mathcal{H}_M)$ denotes the Borel σ -algebra generated by the open sets of \mathcal{H}_M under its norm topology, then $(x, p) \mapsto \langle \Phi_M(x), \Psi_M(p) \rangle_{\mathcal{H}_M}$ is measurable on $\mathcal{F}_{\mathcal{X}_M} \otimes \mathcal{F}_{\mathcal{P}}$.*

Proof sketch: Bochner measurability of Φ_M and Ψ_M implies strong measurability into $\mathcal{B}(\mathcal{H}_M)$; hence $(x, p) \mapsto (\Phi_M(x), \Psi_M(p))$ is measurable on the product σ -algebra. Detailed proof is found in Appendix B.2. \square

Theorem 2 (Multimodal energy-based hallucination formalism). *Between the output and prompt spaces, let the residuals $\mathbf{r}_M(x, p) := \Phi_M(x^{(M)}) - \Psi_M(p) \in \mathcal{H}_M$ be defined for at least two modalities $|\mathcal{M}| \geq 2$. For each M , let there be a bounded, self-adjoint, positive semi-definite (PSD) linear operator A_M on \mathcal{H}_M and for $M \neq M'$, some $B_{MM'} : \mathcal{H}_{M'} \rightarrow \mathcal{H}_M$ which is a bounded linear symmetric cross-operator and a controlled factorization $B_{MM'} = A_M^{1/2} R_{MM'} A_{M'}^{1/2}$, subject to $\|R_{MM'}\| \leq 1$, being a symmetric contraction (e.g., Hilbert–Schmidt). Given this, if the output distribution $f_p(x)$ assumes the Boltzmann form for any temperature $\mathcal{T}_t \in \mathbb{R}_{\geq 0}$ dependent on time $t \in \mathbb{R}^+$:*

$$f_p(x) = (Z(p, \mathcal{T}_t))^{-1} \exp(-\mathcal{E}(x, p)/\mathcal{T}_t), \text{ where, } Z(p, \mathcal{T}_t) = \int_{\mathcal{X}} \exp(-\mathcal{E}(x, p)/\mathcal{T}_t) d\mu(x) \quad (9)$$

is the normalizing partition function, then the total energy noted in Eq. (8), for $(x, p) \in \mathcal{X} \times \mathcal{P}$, takes the form that is measurable, non-negative and satisfies canonical instances; given by:

$$\mathcal{E}(x, p) = \sum_{M \in \mathcal{M}} \langle \mathbf{r}_M, A_M \mathbf{r}_M \rangle_{\mathcal{H}_M} + \frac{2}{|\mathcal{M}| - 1} \sum_{\substack{M, M' \in \mathcal{M} \\ M \neq M'}} \langle A_M^{1/2} \mathbf{r}_M, R_{MM'} A_{M'}^{1/2} \mathbf{r}_{M'} \rangle + \mathcal{E}_{\mathcal{M}}, \quad (10)$$

where the first and second terms on r.h.s are \mathcal{E}_M and $\mathcal{E}_{MM'}$ respectively, while the last term being $\mathcal{E}_{\mathcal{M}}(x, p) = \left\| \bigotimes_{M \in \mathcal{M}} \Phi_M(x^{(M)}) - \bigotimes_{M \in \mathcal{M}} \Psi_M(p) \right\|_{\otimes \mathcal{H}_M}^2$ as a squared distance in composite RKHS, so it's measurable and nonnegative.

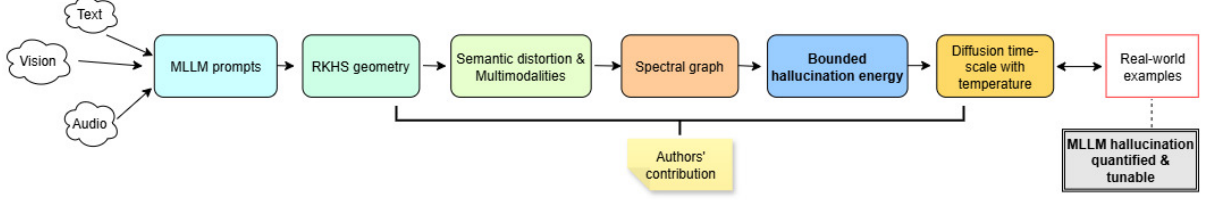


Figure 2: Pipeline for hallucination quantification in MLLMs. For an intuition-building case-study of an image–caption example for an MLLM, see comments^{A.10} in Appendix A.

Proof sketch. We stack $r = (\mathbf{r}_M)_M$ and define the block operator \mathcal{A} with diagonals A_M and off-diagonals $A_M^{1/2} R_{MM'} A_{M'}^{1/2}$. Since $A_M \succeq 0$, $R_{M'M} = R_{MM'}^*$, and $\|R_{MM'}\| \leq 1$, standard Cauchy–Schwarz/Schur arguments give $\mathcal{A} \succeq 0$; hence $\langle r, \mathcal{A}r \rangle \geq 0$ equals the first two terms of Eq. (10). The joint term is a single scalar for 3 modalities, but a tensor for > 3 modalities, thus ≥ 0 . Measurability follows from Bochner measurability and continuity of bounded linear maps/inner products (refer to Lemma 1). Under the stated integrability/finite-measure conditions, the partition function in Eq. (9) is finite, so f_p is well-defined. Detailed proof is found in Appendix B.3. \square

Corollary 1 (Excess-energy hallucination functional). *In line with Theorems 1 & 2, we leverage Eq. (10) to identify the hallucination energy in an MLLM:*

$$\mathcal{E}_{\text{hall}}^{\text{multi}}(x, p, \cdot) = \left(\mathcal{E}(x, p, \cdot) - \mathcal{E}_{\mathcal{K}}(x, p, \cdot) \right)_+ \mathbf{1}_{\{x \notin \mathcal{K}\}}. \quad (11)$$

where $\mathcal{E}(x, p, \cdot)$ is the total energy term at \mathcal{X} and $\mathcal{E}_{\mathcal{K}}(x, p, \cdot)$ is the same restricted at \mathcal{K} .

Proof. This particular Corollary does not require any explicit proof as this is merely an identification done by the authors in line with the results obtained in Theorem 1. \square

5 Main Results: Proposed Framework

In this section we develop the spectral representation that underpins our main results (Figure 2). We reformulate the multimodal hallucination energy $\mathcal{E}_{\text{hall}}^{\text{multi}}$ (refer to Eq. (11)) within standard spectral graph theory [29]. This lets us relate the Boltzmann normalization of model outputs to eigenmodes of a multimodal semantic graph Laplacian, which in turn yields principled mode-wise bounds on hallucination energy.

5.1 Semantic Graph and Multimodal Laplacian

Let a time-indexed, temperature-modulated multimodal semantic knowledge graph at an instant t be:

$$G_{\mathcal{T}_t} = (\mathcal{V}, E, W_{\mathcal{T}_t}), \quad \mathcal{V} \subseteq \mathbb{N}, \quad E \subseteq \mathcal{V} \times \mathcal{V}, \quad W_{\mathcal{T}_t} \in \mathbb{R}^{|\mathcal{V}| \times |\mathcal{V}|}; \quad \forall t \in \mathbb{R}^+, \quad (12)$$

with finite set of nodes \mathcal{V} (semantic units), pairwise edges $E \subseteq \mathcal{V} \times \mathcal{V}$ (similarity relations), and symmetric non-negative adjacency weights $W_{\mathcal{T}_t}$ built from fixed embeddings, where temperature $\mathcal{T}_t \in \mathbb{R}_{\geq 0}$ controls the affinity bandwidths. Here, we adopt a single integrated multimodal graph $G_{\mathcal{T}_t}$ with modality encoded by the node-partitioning $\mathcal{V} = \biguplus_M \mathcal{V}_M$ and a symmetric PSD $W_{\mathcal{T}_t}$ structured on its elements $w_{\mathcal{T}_t}$ noted in Eq. (16) as hyperedge weights. See justification^{A.11} and detailed construction of $W_{\mathcal{T}_t}$ in Appendix A. In the current prescription of \mathcal{T}_t -modulated graph, the RKHS \mathcal{H} is associated with a positive-definite multimodal diffusion kernel $K_{\mathcal{T}_t}$ that induces graph feature map $\Upsilon : \mathcal{V} \rightarrow \mathcal{H}$ satisfying (application of Assumption 4 in knowledge-graphs)

$$K_{\mathcal{T}_t} := \exp\left(-\tau \mathcal{L}_{\mathcal{T}_t}^{\text{multi}}\right), \quad \langle \Upsilon(v), \Upsilon(v) \rangle_{\mathcal{H}} = K_{\mathcal{T}_t}(v, v), \quad \forall v, v \in \mathcal{V}, \quad (13)$$

where $\tau \in \mathbb{R}^+$ is a diffusion time-scale and $\mathcal{L}_{\mathcal{T}_t}^{\text{multi}}$ is a multimodal graph Laplacian defined on the finite node set \mathcal{V} . As an extension from Eq. (7), the above equation is an application of Mercer's theorem [30], see details^{A.12} in Appendix A. How this construction of graph feature maps Υ defined on nodes v, v has an interconnection to the output feature maps $\Phi_M(x^{(M)})$ and prompt embeddings $\Psi_M(p)$, see justification^{A.13} in Appendix A. We design the multimodal Laplacian as a non-negative combination of intra-, cross-, and joint-modal components: $\mathcal{L}_{\mathcal{T}_t}^{\text{multi}} = \sum_* \text{coeff}_* \mathcal{L}_{\mathcal{T}_t}^{(*)}$, where $* \in \{\text{intra}_M, \text{cross}_{MM'}, \text{joint}_M\}$ and the interaction coefficients: $\text{coeff}_{\text{intra}_M} = \alpha_M$ ($\forall M \in \mathcal{M}$), $\text{coeff}_{\text{cross}_{MM'}} = \beta_{MM'} (\forall M, M' \in \mathcal{M})$, and $\text{coeff}_{\text{joint}_M} = \gamma_M$ are all $\mathbb{R}_{\geq 0}$. Each $\mathcal{L}_{\mathcal{T}_t}^{(*)}$ is a symmetric PSD Laplacian-block built on the same node set \mathcal{V} ; full expressions can be found in Eq. (25) in Appendix A.11.

5.2 Spectral Decomposition and Energy Functional

To dis-entangle modality-specific, cross-modal, and joint-modal interactions and to study how hallucination energy propagates across the graph, we diagonalize the normalized multimodal Laplacian. Let $\{(\lambda_i(t), u_i(t))\}_{i=1}^{|\mathcal{V}|}$ be the eigenpairs of $\mathcal{L}_{\mathcal{T}_t}^{\text{multi}}$ with $0 = \lambda_1(t) \leq \lambda_2(t) \leq \dots$ and orthonormal eigenvectors $\langle u_i(t), u_j(t) \rangle = \delta_{ij}$. See comments^{A.14} in Appendix A. Then for all nodes $v \in \mathcal{V}$:

$$\mathcal{L}_{\mathcal{T}_t}^{\text{multi}} = U(t)\Lambda(t)U(t)^\top = \sum_{i=1}^{|\mathcal{V}|} \lambda_i(t) u_i(t) u_i(t)^\top, \quad \Upsilon(v; \mathcal{T}_t) = \sum_{i=1}^{|\mathcal{V}|} e^{-\frac{\tau}{2}\lambda_i(t)} \langle u_i(t), \delta_v \rangle u_i(t), \quad (14)$$

where $U(t) = [u_1(t) \dots u_{|\mathcal{V}|}(t)]$, $\Lambda(t) = \text{diag}(\lambda_1(t), \dots, \lambda_{|\mathcal{V}|}(t))$ and $\delta_v \in \mathbb{R}^{|\mathcal{V}|}$ is the Kronecker delta at v . (We reserve v, v, \dots for graph nodes and i, j, \dots for Laplacian modes; both index sets have size $|\mathcal{V}|$.) For output & prompt nodes $(v_x, v_p) \in \mathcal{V}$ and, more generally, any graph signal $s \in \mathbb{R}^{|\mathcal{V}|}$,

$$\|\Upsilon(v_x; \mathcal{T}_t) - \Upsilon(v_p; \mathcal{T}_t)\|_{\mathcal{H}}^2 = \sum_{i=1}^{|\mathcal{V}|} e^{-\tau\lambda_i(t)} |\langle u_i(t), \delta_{v_x} - \delta_{v_p} \rangle|^2, \quad \langle s, \mathcal{L}_{\mathcal{T}_t}^{\text{multi}} s \rangle = \sum_{i=1}^{|\mathcal{V}|} \lambda_i(t) |\langle u_i(t), s \rangle|^2. \quad (15)$$

A quick algebraic manipulation with Eqs. (15) plugged back into (10) gives the spectral form of total energy: $\mathcal{E}(x, p; \mathcal{T}_t) = \sum_* \sum_{i=1}^{|\mathcal{V}|} \text{coeff}_* E_i^{(*)}(x, p, t)$, where each $E_i^{(*)}$ depends explicitly on $\lambda_i(t)$ and $u_i(t)$. See Eq. (57) in Appendix C.1 for details.

5.3 Spectral bounds on hallucination, and time-decay

Here, we obtain: (i) quantitative bounds that control the scope of hallucination in an MLLM; (ii) an evolution of hallucinations in diffusion time with tunable temperature. The extended derivations of each expression below can be found in Appendix C.2.

Node-level score and pairwise dissimilarity. For each node $v \in \mathcal{V}$ carrying $(x, p) \in \mathcal{X} \times \mathcal{P}$, the scalar score $d_{\text{sem}}^{(\varepsilon, h)}(x | p) := d_{\text{sem}}^{(\varepsilon, h)}(x; \mathcal{K}, \mathcal{X})$ is computed using $\tilde{f}_{p, \varepsilon}$ from Eq. (6). A symmetric, nonnegative prompt-aware dissimilarity between $v_a \sim (x_a, p_a)$ and $v_b \sim (x_b, p_b)$ is then defined by $\hat{d}_{\text{sem}}(v_a, v_b) := |d_{\text{sem}}^{(\varepsilon, h)}(x_a | p_a) - d_{\text{sem}}^{(\varepsilon, h)}(x_b | p_b)|$ and combining it with Eq. (27) yields

$$w_{\mathcal{T}_t}(e) = \mathbf{1}_{\{e \in E^{(*)}\}} \exp \left(-\eta_* \left(\sum_{1 \leq a, b \leq r(e)} |\Delta_{\varepsilon, h}(x_a | p_a) - \Delta_{\varepsilon, h}(x_b | p_b)| \right) / \sum_{a=1}^{r(e)} \mathcal{T}_t(v_a) \right). \quad (16)$$

Here $r(e) := |e|$ is the hyperedge cardinality (Eq. (25)), and $\eta_* > 0$ is the modality-aware permutation factor (Eq. (27)). The derivation of $\Delta_{\varepsilon, h}(x | p)$ is found via Eq. (28) in Appendix A.11.

Courant–Fischer bounds for hallucination. Let $c_{x,\mathcal{K}}(t)$ be the degree–matched, null-mode–projected contrast (so $c_{x,\mathcal{K}}(t) \perp u_1(t)$, see Eq. (58)) and given the diffusion operator $\exp(-2\tau \mathcal{L}_{\mathcal{T}_t}^{\text{multi}})$, we get the semantic diffusion through spectral expansion

$$\langle c_{x,\mathcal{K}}(t), \exp(-2\tau \mathcal{L}_{\mathcal{T}_t}^{\text{multi}}) c_{x,\mathcal{K}}(t) \rangle = \sum_{i=2}^{|\mathcal{V}|} e^{-2\tau \lambda_i(t)} |\langle u_i(t), c_{x,\mathcal{K}}(t) \rangle|^2. \quad (17)$$

By Courant–Fischer principle [31], we get a pure spectral sandwich:

$$e^{-2\tau \lambda_{\max}(t)} \|c_{x,\mathcal{K}}(t)\|^2 \leq \langle c_{x,\mathcal{K}}(t), \exp(-2\tau \mathcal{L}_{\mathcal{T}_t}^{\text{multi}}) c_{x,\mathcal{K}}(t) \rangle \leq e^{-2\tau \lambda_2(t)} \|c_{x,\mathcal{K}}(t)\|^2. \quad (18)$$

By Eq. (57), the full energy is a nonnegative linear combination of blockwise spectral terms, therefore the energy difference admits the eigen-expansion while its spectral weights lie in a bound:

$$\mathcal{E}(x, p; \mathcal{T}_t) - \mathcal{E}_{\mathcal{K}}(x, p; \mathcal{T}_t) = \sum_{i=2}^{|\mathcal{V}|} \zeta_i(t, \tau) |\langle u_i(t), c_{x,\mathcal{K}}(t) \rangle|^2, \quad m(t) e^{-2\tau \lambda_i(t)} \leq \zeta_i(t, \tau) \leq M(t), \quad (19)$$

where $\zeta_i(t, \tau) \geq 0$ and $(m(t), M(t)) \in (0, \infty)$; see Eq.(63) for details. By Eqs. (11), (18) and (19),

$$m(t) e^{-2\tau \lambda_{\max}(t)} \|c_{x,\mathcal{K}}(t)\|^2 \mathbf{1}_{\{x \notin \mathcal{K}\}} \leq \mathcal{E}_{\text{hall}}^{\text{multi}}(x, p, \cdot) \leq M(t) e^{-2\tau \lambda_2(t)} \|c_{x,\mathcal{K}}(t)\|^2 \mathbf{1}_{\{x \notin \mathcal{K}\}}. \quad (20)$$

Calibration-compatible lower envelope for hallucination time-scale. Let $\widehat{m}_{\text{GT}}(t)$ denote the Good–Turing “missing-mass” estimate for the model f_p over $\mathcal{X} \setminus \mathcal{K}$ at time t (computed on the current prompt-conditioned sample window), and we set the calibrated lower-bound aligned with [12] as $\vartheta_{\text{KV}}(t) := \xi \widehat{m}_{\text{GT}}(t)$ for some fixed $\xi \in (0, 1]$. A time-indexed diffusion/temperature profile $\tau = \tau(t)$ is chosen to embed that envelope by identifying

$$m(t) e^{-2\tau(t) \lambda_{\max}(t)} \|c_{x,\mathcal{K}}(t)\|^2 \geq \vartheta_{\text{KV}}(t) \iff \tau(t) \leq \frac{1}{2 \lambda_{\max}(t)} \log \left(\frac{m(t) \|c_{x,\mathcal{K}}(t)\|^2}{\vartheta_{\text{KV}}(t)} \right). \quad (21)$$

Eq. (21) operationalizes Kalai–Vempala’s calibrated lower bound within our spectral framework, guaranteeing the bound is met (and dominated tunably) by the diffusion–Laplacian control.

Time–decay of hallucination energy. From Eq. (20), $\mathcal{E}_{\text{hall}}^{\text{multi}}$ is nonincreasing in τ and decays to 0 as $\tau \rightarrow \infty$ at a rate sandwiched between $e^{-2\tau \lambda_{\max}}$ and $e^{-2\tau \lambda_2}$. When the block responses are diffusion–monotone (standard for normalized kernels), the pointwise derivative exists (for $x \notin \mathcal{K}$)

$$\frac{d}{d\tau} \mathcal{E}_{\text{hall}}^{\text{multi}}(x, p, \cdot) = -2 \sum_{i=2}^{|\mathcal{V}|} \lambda_i(t) \zeta_i(t, \tau) |\langle u_i(t), c_{x,\mathcal{K}}(t) \rangle|^2 \searrow 0, \quad (22)$$

which is compatible with Eq. (19) that makes it implementation-ready.

6 Experiments

Code base. [<REPO>](#). The exact configs used for each run are shipped under `configs/`.

6.1 Datasets and models

We evaluate 3 multimodal datasets crossed with 3 inference stacks, yielding 9 panels (Fig. 3).

Datasets.

- **COCO Captions (val2017)**: large image–text captioning split; diverse everyday scenes.
- **VQAv2**: balanced visual question answering; short free-form answers grounded in images.
- **AudioCaps**: audio–text captioning from YouTube clips; non-visual acoustic events.

Note. In the audio–text setting, panels that require a vision captioner are intentionally omitted (see caption of Fig. 3).

Sources. Pulled from HuggingFace Hub (private tokens); HF_HOME and HF_TOKEN are set at runtime.

Algorithm 1: KL-SMOOTHED MULTIMODAL HALLUCINATION (per prompt p)

Input: $\mathcal{K}; \mu; K_h; \varepsilon, \rho$; blocks $\{\mathcal{I}^{(*)}, E^{(*)}, \omega_*, \eta_*\}; \mathcal{T}_t; \tau; \{\Phi_M, \Psi_M\}_{M \in \mathcal{M}}$;
 $\{A_M\}_M, \{R_{MM'}\}_{M \neq M'}$

Output: $d_{\text{sem}}^{(\varepsilon, h)}(x | p); w_{\mathcal{T}_t}(e); \mathcal{L}_{\mathcal{T}_t}^{\text{multi}}; K_{\mathcal{T}_t}; \mathcal{E}_{\text{hall}}^{\text{multi}}(x, p)$ and CF-bounds

- 1 Form $\tilde{f}_{p, \varepsilon} = (1 - \varepsilon)f_p + \varepsilon\rho$ and $\tilde{f}_{p, \varepsilon}^{\mathcal{K}}$; compute $d_{\text{sem}}^{(\varepsilon, h)}(x | p)$ by Eq. (6). (Thm. 1);
- 2 Compute $\mathbf{r}_M(x, p)$; store $\{A_M, B_{MM'}\}$ for energy in Eq. (10). (Thm. 2);
- 3 Set $\Delta_a = d_{\text{sem}}^{(\varepsilon, h)}(x_a | p)$ and $w_{\mathcal{T}_t}(e)$ by Eq. (27); build $\mathcal{L}_{\mathcal{T}_t}^{(*)}$ via Eq. (25) and assemble $\mathcal{L}_{\mathcal{T}_t}^{\text{multi}}$ via Eq. (26);
- 4 Compute $K_{\mathcal{T}_t}$ and set graph features $\Upsilon(v)$ so that $\langle \Upsilon(v), \Upsilon(v) \rangle_{\mathcal{H}} = K_{\mathcal{T}_t}(v, v)$ (Eq. (14));
- 5 Form $c_{x, \mathcal{K}}(t)$ by Eq. (58) and apply bounds in Eq. (18);
- 6 Evaluate $\mathcal{E}(x, p)$ via Eq. (10); set $\mathcal{E}_{\text{hall}}^{\text{multi}}$ by Eq. (11); report Courant–Fischer bounds in Eq. (20) plus KV/Good–Turing calibration via Eq. (21);;
- 7 **return** $d_{\text{sem}}^{(\varepsilon, h)}, w_{\mathcal{T}_t}(e), \mathcal{L}_{\mathcal{T}_t}^{\text{multi}}, K_{\mathcal{T}_t}, \mathcal{E}_{\text{hall}}^{\text{multi}}$ (with bounds)

Algorithm	COCO AUROC / AUPRC	VQAv2 AUROC / AUPRC	AudioCaps AUROC / AUPRC	Avg. AUROC / AUPRC
Entropy	0.81 / 0.79	0.78 / 0.75	0.74 / 0.70	0.78 / 0.75
MaxProb	0.82 / 0.81	0.80 / 0.77	0.76 / 0.72	0.79 / 0.77
Margin	0.83 / 0.82	0.81 / 0.78	0.77 / 0.74	0.80 / 0.78
$d_{\text{sem}}^{(\varepsilon, h)}$ (ours)	0.86 / 0.84	0.84 / 0.81	0.80 / 0.77	0.83 / 0.81

Model	COCO median (lo / hi)	VQAv2 median (lo / hi)	AudioCaps median (lo / hi)	Avg. median	Throughput ex/s	Asymp.
CLIP+Whisper+T5	2.11 (0.42 / 3.05)	2.23 (0.50 / 3.28)	2.35 (0.55 / 3.50)	2.23	420	$O(E + N \log k + md)$
BLIP+CLIP+Whisper	1.98 (0.40 / 2.90)	2.05 (0.48 / 2.96)	—	2.02	360	$O(E + N \log k + md)$
SigLIP+Whisper+T5	1.92 (0.38 / 2.85)	1.99 (0.45 / 2.90)	2.08 (0.50 / 3.05)	2.00	400	$O(E + N \log k + md)$

Table 1: (a) **Detection (AUROC/AUPRC)** and (b) **Energy diagnostics with runtime**. **Bold** = column-best; in (b), lower median energy is better and throughput (ex/s) higher is better. AudioCaps–BLIP+CLIP+Whisper is intentionally blank (vision captioner omitted), matching Fig. 3.

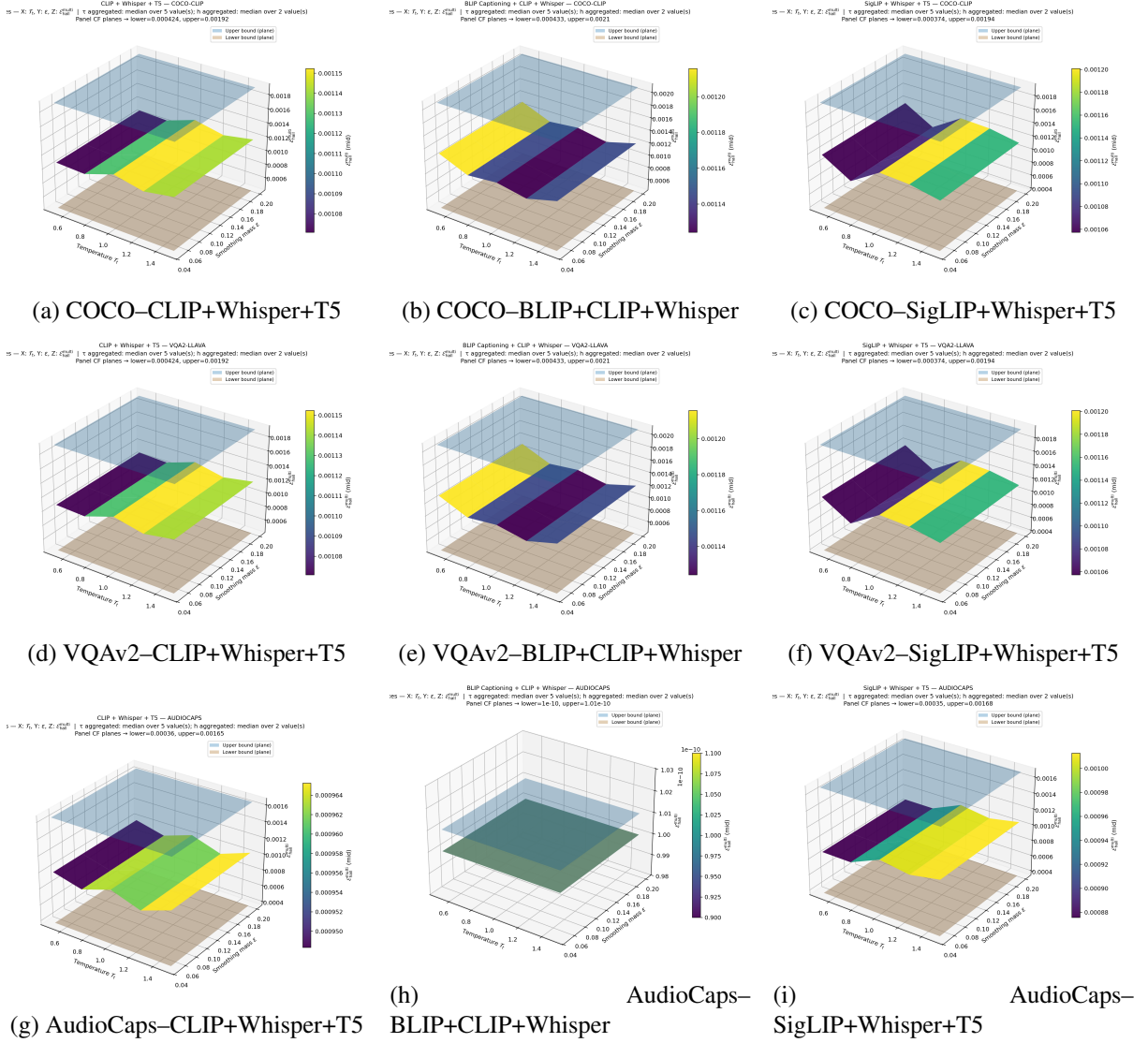


Figure 3: **CF-bounded hallucination energy surfaces (9 panels).** Each 3D surface shows $\mathcal{E}_{\text{hall}}^{\text{multi}}$ over temperature T_t (X) and smoothing mass ε (Y), clamped between two panel-specific parallel planes marking the Courant–Fischer lower (strictly > 0) and upper bounds (Z). Other hyperparameters (τ, h) are aggregated by median, consistent across panels. *Note:* the **AudioCaps–BLIP+CLIP+Whisper** panel may appear blank if the BLIP vision backbone is intentionally omitted for the audio–text setup; this is expected and documented in our pipeline.

6.2 Metrics and evaluation

We report AUROC/AUPRC for hallucination detection using $d_{\text{sem}}^{(\varepsilon, h)}$ against entropy, max-probability, and margin baselines, and summarize CF-bounded energy surfaces (lower is better) with temperature/ ε trends matching theory. Details about the baselines and all remaining protocol & design, and compute details are found in Appendix D.

7 Conclusion and Future Work

We proposed a reference-free, KL-smoothed information gap with hypergraph–spectral control: the score is 0 on \mathcal{K} and strictly > 0 off \mathcal{K} , admits Courant–Fischer (CF) bounds, and integrates Good–Turing/KV calibration. Compact Colab runs (COCO/VQAv2/AudioCaps \times CLIP/BLIP/SigLIP stacks)

show consistent gains over entropy/margin and interpretable temperature/ τ decay. A joint tuning of $(\varepsilon, h, \mathcal{T}_t, \tau)$ with uncertainty can be the next direction.

Acknowledgments

SS gratefully acknowledges the organizational leadership support for AI research from both local and functional spaces: *Arijit Das* (Executive Director, Morgan Stanley) and *Sudha Sukumaran Kamonjoh* (Managing Director, Morgan Stanley) respectively. SS also extends sincere thanks to *Debanjan Dutta* (Indian Statistical Institute, Kolkata) for numerous insightful academic discussions that helped shape the trajectory of this work, *Arindam Khan* (Indian Institute of Science, Bengaluru) for his initial guidance in theoretical computer science, and *Subrata Mitra* (Adobe Research) for his valuable advice on prospective research directions, particularly in the field of LLMs.

References

- [1] Ziwei Ji, Nayeon Lee, Rita Frieske, Tiezheng Yu, Dan Su, Yan Xu, Etsuko Ishii, Yejin Bang, Andrea Madotto, and Pascale Fung. Survey of hallucination in natural language generation. *ACM Computing Surveys*, 55(12):1–38, 2023.
- [2] Justin Maynez, Shashi Narayan, Bernd Bohnet, and Ryan McDonald. On faithfulness and factuality in abstractive summarization. In *Proceedings of the Annual Meeting of the Association for Computational Linguistics (ACL)*, pages 1906–1919, 2020.
- [3] Sébastien Bubeck, Varsha Chandrasekaran, Ran Eldan, Johannes Gehrke, Eric Horvitz, Ece Kamar, Percy Lee, Yu Li, Scott Lundberg, Harsha Nori, et al. Sparks of artificial general intelligence: Early experiments with gpt-4. Technical report, arXiv, 2023. arXiv preprint arXiv:2303.12712.
- [4] Peng Ding, X. Hu, H. Li, X. Chen, and H. Ji. Hallu-pi: Benchmarking hallucinations under perturbed inputs for large language models. In *ICLR*, 2024.
- [5] T. Bai, Y. Zhang, X. Lin, Q. Sun, and C. Wu. Multimodal hallucinations: A survey of causes, metrics, and mitigation. Technical report, arXiv, 2024. arXiv:2404.18930.
- [6] C. Jiang, B. Qi, X. Hong, D. Fu, Y. Cheng, F. Meng, M. Yu, B. Zhou, and J. Zhou. On large language models’ hallucination with regard to known facts. In *NAACL*, 2024.
- [7] X. Wang, Y. Yan, L. Huang, X. Zheng, and X. Huang. Hallucination detection for generative large language models by bayesian sequential estimation. In *EMNLP*, pages 15361–15371, 2023.
- [8] J. Han, J. Kossen, M. Razzak, L. Schut, S. Malik, and Y. Gal. Semantic entropy probes: Robust and cheap hallucination detection in large language models. In *ICML Workshop on Foundation Models in the Wild*, 2024.
- [9] S. Park, X. Du, M.-H. Yeh, H. Wang, and S. Li. Steer llm latents for hallucination detection. Technical report, ICML Poster, 2025.
- [10] G. Sun, P. Manakul, A. Liusie, K. Pipatanakul, C. Zhang, P. Woodland, and M. Gales. Crosscheck-gpt: Universal hallucination ranking for multimodal foundation models. In *NeurIPS Workshop on Next Gen Multimodal Models*, 2024.
- [11] J. Xie, C. Zhang, and M. Li. Spectral characterization of hallucination in large language models. Technical report, arXiv, 2025. arXiv:2502.17598.

- [12] Adam Tauman Kalai and Santosh S. Vempala. Calibrated language models must hallucinate. In *Proceedings of the 56th Annual ACM Symposium on Theory of Computing (STOC)*, pages 160–171, 2024.
- [13] Adam Tauman Kalai, Ofir Nachum, Santosh S. Vempala, and Edwin Zhang. Why language models hallucinate. *arXiv preprint arXiv:2509.04664*, 2025.
- [14] Adly Templeton, Tom Conerly, Jonathan Marcus, Jack Lindsey, Trenton Bricken, Brian Chen, Adam Pearce, Craig Citro, Emmanuel Ameisen, Andy Jones, Hoagy Cunningham, Nicholas L. Turner, Callum McDougall, Monte MacDiarmid, C. Daniel Freeman, Theodore R. Sumers, Edward Rees, Joshua Batson, Adam Jermyn, Shan Carter, Chris Olah, and Tom Henighan. Scaling monosemanticity: Extracting interpretable features from claude 3 sonnet. Transformer Circuits Thread, 2024. Anthropic Interpretability Team.
- [15] Assaf Gerner, Netta Madvil, Nadav Barak, Alex Zaikman, Jonatan Liberman, Liron Hamra, Rotem Brazilay, Shay Tsadok, Yaron Friedman, Neal Harow, Noam Bressler, Shir Choref, and Philip Tannor. Orion grounded in context: Retrieval-based method for hallucination detection. *arXiv preprint arXiv:2504.15771*, 2025.
- [16] Chenxi Niu et al. Ragtruth: A hallucination corpus for developing more truthful systems. In *ACL*, 2024.
- [17] Jiaan Li et al. Halueval: A large-scale hallucination evaluation benchmark for llms. In *EMNLP*, 2023.
- [18] Tao Feng, Yihang Sun, and Jiaxuan You. Grapheval: A lightweight graph-based llm framework for idea evaluation. *arXiv preprint arXiv:2503.12600*, 2025.
- [19] Anna Rohrbach et al. Object hallucination in image captioning. In *EMNLP*, 2018.
- [20] Vipula Rawte, Swagata Chakraborty, Agnibh Pathak, Anubhav Sarkar, S. M. Towhidul Islam Tommoy, Aman Chadha, Amit Sheth, and Amitava Das. The troubling emergence of hallucination in large language models: An extensive definition, quantification, and prescriptive remediations. In *Proceedings of the 2023 Conference on Empirical Methods in Natural Language Processing*, pages 2541–2573, Singapore, 2023. Association for Computational Linguistics.
- [21] Seongmin Lee, Hsiang Hsu, and Chun-Fu Chen. Llm hallucination reasoning with zero-shot knowledge test. *arXiv preprint arXiv:2411.09689*, 2024.
- [22] Potsawee Manakul, Adian Liusie, and Mark J. F. Gales. Selfcheckgpt: Zero-resource black-box hallucination detection for generative large language models. In *Proceedings of EMNLP*, 2023.
- [23] Albert Sawczyn, Jakub Binkowski, Denis Janiak, Bogdan Gabrys, and Tomasz Kajdanowicz. Fact-selfcheck: Fact-level black-box hallucination detection for llms. *arXiv preprint arXiv:2503.17229*, 2025.
- [24] Jakub Binkowski, Denis Janiak, Albert Sawczyn, Bogdan Gabrys, and Tomasz Kajdanowicz. Spectral characterization of hallucination in large language models. *arXiv preprint arXiv:2502.17598*, 2025.
- [25] Eric Le Merrer and Gilles Trédan. Llms hallucinate graphs too: A structural perspective. *arXiv preprint arXiv:2409.00159*, 2024.
- [26] Terence Tao. *An Introduction to Measure Theory*, volume 126 of *Graduate Studies in Mathematics*. American Mathematical Society, 2011. Covers sigma-algebras, outer measures, completeness, and constructions of measure.

- [27] Robert G. Bartle. *The Elements of Integration and Lebesgue Measure*. Wiley-Interscience, corrected reprint of the 1st ed. (1966) edition, 1995. Introduction emphasizing Lebesgue measure on \mathbb{R}^n with clarity and examples.
- [28] Nachman Aronszajn. Theory of reproducing kernels. *Transactions of the American Mathematical Society*, 68(3):337–404, 1950.
- [29] Fan R. K. Chung. *Spectral Graph Theory*, volume 92 of *CBMS Regional Conference Series in Mathematics*. American Mathematical Society, Providence, RI, 1997.
- [30] James Mercer. Functions of positive and negative type, and their connection with the theory of integral equations. *Philosophical Transactions of the Royal Society A*, 209:415–446, 1909.
- [31] Roger A. Horn and Charles R. Johnson. *Matrix Analysis*. Cambridge University Press, Cambridge, 2 edition, 2013.
- [32] Alec Radford et al. Learning transferable visual models from natural language supervision. *arXiv:2103.00020*, 2021.
- [33] Alec Radford et al. Learning transferable visual models from natural language supervision. In *Proceedings of the 38th International Conference on Machine Learning*, 2021.
- [34] Y. Zhang et al. Semantics at an angle: When cosine similarity works until it doesn’t. *arXiv:2504.16318*, 2025.
- [35] Ashish Vaswani et al. Attention is all you need. In *NeurIPS*, 2017.
- [36] Rico Sennrich, Barry Haddow, and Alexandra Birch. Neural machine translation of rare words with subword units. In *ACL*, 2016.
- [37] Taku Kudo and John Richardson. Sentencepiece: A simple and language independent subword tokenizer and detokenizer for neural text processing. *arXiv:1808.06226*, 2018.
- [38] Christopher K. I. Williams and Matthias Seeger. Using the nyström method to speed up kernel machines. In *Advances in Neural Information Processing Systems (NeurIPS)*, 2001.
- [39] Ali Rahimi and Benjamin Recht. Random features for large-scale kernel machines. In *Advances in Neural Information Processing Systems (NeurIPS)*, 2007.
- [40] Andrew Y. Ng, Michael I. Jordan, and Yair Weiss. On spectral clustering: Analysis and an algorithm. In *NeurIPS*, 2002.
- [41] R. R. Coifman and S. Lafon. Diffusion maps. *Applied and Computational Harmonic Analysis*, 2006.
- [42] Lihi Zelnik-Manor and Pietro Perona. Self-tuning spectral clustering. In *NeurIPS*, 2004.
- [43] Geoffrey Hinton, Oriol Vinyals, and Jeff Dean. Distilling the knowledge in a neural network. In *NeurIPS Deep Learning Workshop*, 2015.
- [44] Dengyong Zhou, Jiayuan Huang, and Bernhard Schölkopf. Learning with hypergraphs: Clustering, classification, and embedding. *Advances in Neural Information Processing Systems*, 19:1601–1608, 2006.
- [45] Joseph Diestel and Jr. John J. Uhl. *Vector Measures*, volume 15 of *Mathematical Surveys and Monographs*. American Mathematical Society, 1977.

Appendix

In this section, we provide elaboration on footnotes, extended derivations of our Theorems, some supplementary mathematical results, and details of experimental validation.

A Technical Notes and Extended Comments

Here, we provide elaboration on footnotes/ some extended explanations.

A.1 Measurable Sets and σ -algebra

Any mathematical set can be equipped with a σ -algebra to form a measurable space, say, \mathcal{X} . The common choices are: (i) the power set if \mathcal{X} is countable/ finite, (ii) the Borel σ -algebra if \mathcal{X} is a topological space (e.g., continuous embeddings), (iii) Product σ -algebra if \mathcal{X} is a product of spaces (e.g., sequences of tokens or multimodal outputs). For a measure space $(\mathcal{X}, \mathcal{F}_{\mathcal{X}}, \mu)$ and $1 \leq p < \infty$ (where p is the integrability exponent, not to be clashed with “prompts”), the space $L^p(\mathcal{X}, \mathcal{F}_{\mathcal{X}}, \mu)$ consists of (equivalence classes of) μ -measurable $q : \mathcal{X} \rightarrow \mathbb{R}$ with $\int_{\mathcal{X}} |q(x)|^p d\mu(x) < \infty$; the norm is $\|q\|_{L^p} := (\int |q|^p d\mu)^{1/p}$. For $p = \infty$, L^∞ denotes essentially bounded functions with norm $\|q\|_{L^\infty} := \text{ess sup}_x |q(x)|$. In particular, L^1 denotes integrable functions ($p = 1$).

A.2 Ground truth distribution

The absence of an exact analytical expression of $g(x)$ limits the direct interpretability, but provides a flexible framework for comparing the model outputs to the ground-truth via the functional and spectral metrics. This is used only as a theoretical reference for calibration/fidelity analyses representing the (idealized) generative distribution of facts/outputs as seen in [12].

A.3 Definition of KL-divergence

For any two probability distributions $P_1(x)$ and $P_2(x)$, say defined over the same space $x \in \mathcal{X}$, the functional operator $D_{\text{KL}} \in \mathbb{R}_{\geq 0}$ refers to the KL divergence of $P_2(x)$ from the “true” reference or actual distribution $P_1(x)$ as:

$$D_{\text{KL}}(P_1(x) \parallel P_2(x)) = \sum_{x \in \mathcal{X}} P_1(x) \log \frac{P_1(x)}{P_2(x)}.$$

When x is a continuous random variable, $\sum_{x \in \mathcal{X}}$ is evidently replaced by $\int_{x=-\infty}^{\infty}$ with $P_1(x)$ & $P_2(x)$ by respective probability densities. More generally, if P_1 & P_2 are probability measures on a measurable space \mathcal{X} , then

$$D_{\text{KL}}(P_1 \parallel P_2) = \int_{x=-\infty}^{\infty} P_1(dx) \log \frac{P_1(dx)}{P_2(dx)},$$

where $\frac{P_1(dx)}{P_2(dx)}$ is the Radon–Nikodym derivative of P_1 w.r.t P_2 .

A.4 Absence of the “ground-truth”

Even without access to g , one can (i) estimate $\mathbb{P}_{f_p}(\mathcal{K})$ from samples, (ii) compute per-instance distortions via the log-likelihood ratio, and (iii) aggregate these into empirical bounds and diagnostics. In multimodal settings, the same decomposition localizes contributions by modality and by interaction (intra/cross/joint), enabling targeted interventions—e.g., modality-specific calibration, cross-modal consistency constraints, or temperature schedules—and straightforward experimental verification via ablations that track how $\mathbb{P}_{f_p}(\mathcal{K})$ and the induced distortions respond to each mitigation.

A.5 Modalities in Expanded Forms

In multi-modal settings, the LLM outputs involve textual (T), visual (V), audio (A) modalities and, for better understanding, Eq. (7) can also be re-written as:

$$\begin{aligned}\mathcal{X} : \mathcal{X}_T \times \mathcal{X}_V \times \mathcal{X}_A, \quad x = (x^{(T)}, x^{(V)}, x^{(A)}), \quad \mathcal{H} := \mathcal{H}_T \otimes \mathcal{H}_V \otimes \mathcal{H}_A, \\ K(x_1, x_2) = K_T(x_1^{(T)}, x_2^{(T)}) \cdot K_V(x_1^{(V)}, x_2^{(V)}) \cdot K_A(x_1^{(A)}, x_2^{(A)}), \\ \mathcal{P} : \mathcal{P}_T \times \mathcal{P}_V \times \mathcal{P}_A, \quad p = (p^{(T)}, p^{(V)}, p^{(A)}).\end{aligned}\tag{23}$$

A.6 Explanation on hallucination energy

As noted in Eq.(8) in Section 4.3, three terms are: (i) \mathcal{E}_M encodes the intra-modal contributions, (ii) $\mathcal{E}_{MM'}$ captures the pairwise cross-modal terms, while (iii) \mathcal{E}_M being the joint contribution of all three modalities combined. For three modalities, (i) & (ii) form an energy matrix of order 3 with diagonals \mathcal{E}_M and off-diagonals $\mathcal{E}_{MM'}$, while \mathcal{E}_M is a single joint term. With > 3 modalities, \mathcal{E}_M becomes a higher order tensor. This structure not only reveals which modality interactions contribute the most to the semantic drift $d_{\text{sem}}(x; \mathcal{K}, \mathcal{X})$, also enables deriving tight spectral bounds on hallucination energy, which would be impossible under a monolithic energy formulation.

A.7 Explicit justification for Assumptions 4 & 5

For Assumptions 4: this mirrors common practice: modern encoders (CLIP, BERT-style, vision backbones) apply normalization or LayerNorm, and we L2-normalize final vectors so magnitudes stay well-behaved. Bounded features make cosine/similarity scores comparable across modalities, prevent numerical outliers, and keep spectral/energy measures meaningful. In deployment, this is easy to enforce (normalize outputs) and verify (log histograms/max norms and alert on drift). Production stacks (vector DBs, ANN indices, faiss/scann) expect bounded vectors so cosine similarity behaves predictably and distances are comparable across batches and time.

- **Why we need this:** For numerical stability to prevent overflow/NaNs and keep the dot products/similarities in a usable range during training and evaluation and comparability across modalities to handle text & image embeddings simultaneously.
- **Real-world example:** Modern vision–language encoders (e.g., CLIP) explicitly L2-normalize image/text embeddings and use cosine similarity with temperature-scaled softmax, so representation norms are controlled by design; this makes cross-modal scoring numerically stable and comparable out of the box [32–34].

For Assumption 5: it is reasonable to assume small prompt edits should not cause large representational jumps - matching real product needs for predictable UX, reproducible evaluation, and reduced prompt-sensitivity exploits. In practice, prompt encoders are compositions of linear layers + pointwise activations + norm layers; we also L2-normalize the final embedding.

- **Why we need this:** If “Adding a comma” or “Swapping a synonym” flips the model’s answer, the system feels brittle. Stability is essential for predictability and debuggability.
- **Real-world example:** Text prompts are tokenized into a finite vocabulary (BPE/WordPiece/SentencePiece), and the transformer encoder maps these tokens through a sequence of standard layers to probabilities via softmax, yielding well-defined distributions on a discrete space—hence measurability is immediate and commonplace [35–37]. Length caps, normalization, and regularization used in real systems keep prompt embeddings within reasonable ranges and make small paraphrases produce small representational changes, which is precisely the stability we assume.

A.8 Feature Maps in RKHS

RKHS theory is rooted in Hilbert space theory (inner product spaces of functions) and uses results like the Moore–Aronszajn theorem [28]). In Measure Theory & Probability, when kernels are used for distributions (e.g., kernel mean embeddings), the feature map connects to integration theory and probabilistic representations. In Machine Learning, the feature maps are used in kernel methods (in practice: SVMs, Gaussian processes, etc.), making this concept central to the theory of statistical learning (e.g., RKHS regularization). Let Φ_M be a feature map (i.e., identified as a function) such that

$$K_M(x_1^{(M)}, x_2^{(M)}) = \langle \Phi_M(x_1^{(M)}), \Phi_M(x_2^{(M)}) \rangle_{\mathcal{H}_M}, \quad (24)$$

embedding raw objects, say outputs (x_1, x_2) , into the modality-specific RKHS \mathcal{H}_M . Instead of just outputs, it can very well mix with the inputs as well meaning: (x, p) . Eq. (24) makes this RKHS \mathcal{H}_M unique up to isometry according to the Moore–Aronszajn theorem.

In classical ML, we use “features” to describe the structured attributes of the input data (e.g., pixel values, word embeddings etc.). In the theory of kernels, the feature maps are abstract (possibly infinite), but they play the same role: they represent the data in a space where linear methods (dot products) can capture nonlinear similarities. Thus, Φ_M allows nonlinear learning algorithms to operate in a high-dimensional feature space of an MLLM via the kernel trick.

In practice, implementations typically compute K_M directly—or via finite approximations like Nyström [38] or Random Fourier Features [39] - so Φ_M need not be explicitly materialized.

A.9 Justification for Assumption 6

In practice, an MLLM scores a finite candidate set $C(x, p)$ (beam/nucleus/reranked hypotheses) via logits or similarity, so with counting measure and energy $\mathcal{E} = -\text{logit}$ (or a bounded margin), the induced softmax probability $\text{prob.}(c | x, p; \mathcal{T}_t) \propto \exp(-\mathcal{E}(c)/\mathcal{T}_t)$ is exactly a Boltzmann distribution with finite partition function $Z = \sum_{c \in C} \exp(-\mathcal{E}(c)/\mathcal{T}_t)$ —hence both operationally realistic and mathematically well-posed.

A.10 An Example (image–caption pair)

One can consider an MLLM generating a caption for an image. Let \mathcal{X} be the space of all captions, with $\mathcal{K} \subseteq \mathcal{X}$ denoting those grounded in the image (e.g., “A cat on a sofa”), while f_p may also assign mass outside \mathcal{K} to hallucinated captions (e.g., “A dog playing with a ball”). The hallucination divergence $D_{\text{KL}}(g \| f_p)$ quantifies this deviation.

In this paper, as a part of our main theoretical contributions, we define a multimodal graph whose nodes are caption tokens T and image patches V , with edge weights $W_{\mathcal{T}_t}(i, j)$ computed from the fixed embeddings and modulated by a time-varying temperature \mathcal{T}_t . From these weights, we will define the normalized multimodal Laplacian $\mathcal{L}_{\mathcal{T}_t}^{\text{multi}}$ associated with a spectral grounding energy as the quadratic form of $\mathcal{L}_{\mathcal{T}_t}^{\text{multi}}$ evaluated on the residual feature field induced by our energy prescription. It helps reveal how hallucination energy is distributed across the modes (e.g., textual vs. cross-modal misalignment).

A.11 Graph notations and Adjacency Weights

In Eq. (12) noted in Section 5.1, \mathcal{V} is the finite set of nodes, E is the set of edges, and $W_{\mathcal{T}_t}$ is a temperature-modulated, symmetric, non-negative, weighted adjacency matrix (zero diagonal) introduced to assign different weights to the edges (indexed by E). We consider either a node-wise local schedule $\mathcal{T}_t : \mathcal{V} \rightarrow \mathbb{R}^+$ in which the edge temperatures are combined symmetrically to keep $W_{\mathcal{T}_t}$ symmetric or a global scalar schedule (\mathcal{T}_t constant over \mathcal{V}). Here, each node represents a semantic unit (e.g., concepts, tokens, ideas), and edges represent the semantic similarity. The multimodal structure is represented by a disjoint partition of the node set $\mathcal{V} = \bigsqcup_{M \in \mathcal{M}} \mathcal{V}_M$ and corresponding within- and cross-modal blocks of $W_{\mathcal{T}_t}$ which is constructed from fixed modality embeddings via temperature-controlled

similarity functions. Lower \mathcal{T}_t yields more localized (sharper) affinities; higher \mathcal{T}_t diffuses those (or, in other words, induces more “noise”). This is a standard property under any temperature-scaled affinity constructions - e.g., Gaussian/RBF kernels with bandwidth proportional to \mathcal{T}_t or softmax similarities with temperature \mathcal{T}_t [29, 40–43]. Thus, the temperature \mathcal{T}_t dynamically modulates the graph edge connectivity and semantic distortion d_{sem} noted in Theorem 1 and, being a time-indexed function, captures the semantic evolution or uncertainty drift across the graph nodes as knowledge updates over time t .

Here, we drop the explicit modality subscripts in Eq. (12), as the modality information is carried by a fixed partition of the vertex set $\mathcal{V} = \biguplus_{M \in \mathcal{M}} \mathcal{V}_M$ together with the block structure of the temperature-modulated weights $W_{\mathcal{T}_t}$, so we do not maintain separate graphs per modality. We assume $W_{\mathcal{T}_t}$ to be symmetric, non-negative, and zero on the diagonal, with \mathcal{T}_t acting as a bandwidth/temperature schedule that controls the locality of affinities. From $W_{\mathcal{T}_t}$, we define the normalized multimodal Laplacian $\mathcal{L}_{\mathcal{T}_t}^{\text{multi}}$ in Section 5.1 and design it to be symmetric and PSD by construction; its spectral decomposition yields an orthonormal basis of eigenmodes together with nonnegative eigenvalues. We interpret each mode by its loadings on the partition $\{\mathcal{V}_M\}_{M \in \mathcal{M}}$: some modes are concentrated on a single modality (text, vision, or audio), while others are cross-modal mixtures that capture interactions between partitions. These modes serve as canonical coordinates for representing the residual signal induced by the energy model and for attributing hallucination energy across modality-specific and cross-modal directions. We use this spectral basis to define propagation in time (via diffusion generated by $\mathcal{L}_{\mathcal{T}_t}^{\text{multi}}$) and to derive mode-wise bounds that connect the Boltzmann formulation to spectral-graph structure in a implementable manner.

Hypergraph blocks and effective pairwise adjacency. To accommodate > 2 modalities, we construct each interaction block via the normalized hypergraph Laplacian [44]:

$$\begin{aligned} \mathcal{L}_{\mathcal{T}_t}^{(*)} &= \mathbf{I} - (\mathcal{D}_{v, \mathcal{T}_t}^{(*)})^{-1/2} \underbrace{(\mathcal{I}^{(*)} W_{\mathcal{T}_t}^{(*)} (\mathcal{D}_{e, \mathcal{T}_t}^{(*)})^{-1} (\mathcal{I}^{(*)})^\top)}_{W_{\mathcal{T}_t}^{*, \text{eff}}} (\mathcal{D}_{v, \mathcal{T}_t}^{(*)})^{-1/2}, \\ \mathcal{D}_{v, \mathcal{T}_t}^{(*)} &= \text{diag}(\{\mathfrak{d}_{\mathcal{T}_t}^{(*)}(v)\}_{v \in \mathcal{V}}), \quad \mathfrak{d}_{\mathcal{T}_t}^{(*)}(v) = \sum_{e \in E^{(*)}} w_{\mathcal{T}_t}(e) \mathcal{I}^{(*)}(v, e), \\ \mathcal{D}_{e, \mathcal{T}_t}^{(*)} &= \text{diag}(\{r(e)\}_{e \in E^{(*)}}), \quad r(e) = |e| \text{ (hyperedge cardinality)}, \\ \mathcal{I}^{(*)} &\in \{0, 1\}^{|\mathcal{V}| \times |E^{(*)}|} \text{ (node-hyperedge incidence)}, \quad W_{\mathcal{T}_t}^{(*)} = \text{diag}(\{w_{\mathcal{T}_t}(e)\}_{e \in E^{(*)}}), \\ \forall * &\in \{\text{intra}_M, \text{cross}_{MM'}, \text{joint}_M\}, \quad \forall v \in \mathcal{V} \text{ (graph nodes)}. \end{aligned} \tag{25}$$

Here \mathbf{I} is the $|\mathcal{V}| \times |\mathcal{V}|$ identity. To be noted that

- (i) v runs over the graph nodes, and no roles attached yet. Output or prompt embeddings are later designated roles on the nodes: $v_x, v_p \in \mathcal{V}$ only while forming the contrast $c_{x, \mathcal{K}}(t)$ seen in Eq.(58). Thus, $\mathcal{L}_{\mathcal{T}_t}^{(*)}$ itself is designed to be role-agnostic.
- (ii) E^* denotes the hyperedge set used to build each interaction block $(*)$ above, while E still remains consistent as per Eq.(12). $r(e)$ is the number of nodes in the hyperedge e ; i.e., $e = \{v_1, \dots, v_{r(e)}\} \subset \mathcal{V}$.
- (iii) $\mathcal{D}_{v, \mathcal{T}_t}^{(*)}$ is the node-degree matrix (of size $|\mathcal{V}| \times |\mathcal{V}|$) for block $*$: it is diagonal with entries $(\mathcal{D}_{v, \mathcal{T}_t}^{(*)})_{vv} = \mathfrak{d}_{\mathcal{T}_t}^{(*)}(v)$, the temperature-weighted degree of node v computed from the hyperedge weights in that block.
- (iv) $\mathcal{D}_{e, \mathcal{T}_t}^{(*)}$ is the hyperedge-cardinality matrix (of size $|E^{(*)}| \times |E^{(*)}|$) for block $*$: it is diagonal with entries $(\mathcal{D}_{e, \mathcal{T}_t}^{(*)})_{ee} = r(e)$.
- (v) The node set \mathcal{V} is fixed; $r(e)$ is a property of each hyperedge $e \subset \mathcal{V}$ and is independent of $|\mathcal{V}|$ (and of the number of modalities $|\mathcal{M}|$ unless joint hyperedges are specifically chosen to include one node per modality).

The matrix $W_{\mathcal{T}_t}^{(*), \text{eff}} = \mathcal{I}^{(*)} W_{\mathcal{T}_t}^{(*)} (\mathcal{D}_{e, \mathcal{T}_t}^{(*)})^{-1} (\mathcal{I}^{(*)})^\top$ is the “effective” pairwise adjacency induced by hyperedges (zero diagonal by convention). The pairwise quantities in Eq. (12) are then obtained by summing blocks:

$$W_{\mathcal{T}_t} = \sum_* \omega_* W_{\mathcal{T}_t}^{(*), \text{eff}}, \quad \omega_* \geq 0 \text{ (absorbed by interaction coefficients } \alpha_M, \beta_{MM'}, \gamma_{\mathcal{M}} \text{).} \quad (26)$$

We pick any two nodes: say, v_a, v_b in the hyperedge $e = \{v_1, \dots, v_a, \dots, v_b, \dots, v_{r(e)}\} \subset \mathcal{V}$ to define a symmetric, nonnegative pairwise dissimilarity $\hat{d}_{\text{sem}}(v_a, v_b)$. This quantity captures the semantic distortion at node level.

For some modality-aware permutation factor η_* , a generic choice of $w_{\mathcal{T}_t}(e)$ is

$$w_{\mathcal{T}_t}(e) = \mathbf{1}_{\{e \in E^{(*)}\}} \exp \left(-\eta_* \frac{\sum_{\substack{1 \leq v_a, v_b \leq r(e) \\ 1 \leq v_a \leq r(e)}} \hat{d}_{\text{sem}}(v_a, v_b)}{\sum_{1 \leq v_a \leq r(e)} \mathcal{T}_t(v_a)} \right), \quad (27)$$

which is permutation-invariant and temperature-scaled.

$$\begin{aligned} \Delta_{\varepsilon, h}(x \mid p) := & \left[\log \left(\frac{\int_{\mathcal{K}} K_h(\Pi_{\mathcal{K}}(x), x_2) \left[(1 - \varepsilon) Z(p, \mathcal{T}_t)^{-1} e^{-\mathcal{E}(x_2, p)/\mathcal{T}_t} + \varepsilon \rho(x_2) \right] d\mu(x_2)}{\int_{\mathcal{K}} \left[(1 - \varepsilon) Z(p, \mathcal{T}_t)^{-1} e^{-\mathcal{E}(x_2, p)/\mathcal{T}_t} + \varepsilon \rho(x_2) \right] d\mu(x_2)} \right) \right. \\ & \left. - \log \left(\int_{\mathcal{X}} K_h(x, x_2) \left[(1 - \varepsilon) Z(p, \mathcal{T}_t)^{-1} e^{-\mathcal{E}(x_2, p)/\mathcal{T}_t} + \varepsilon \rho(x_2) \right] d\mu(x_2) \right) \right]_+, \end{aligned} \quad (28)$$

A.12 Mercer’s theorem

By Mercer’s theorem [30], if $K_{\mathcal{T}_t}$ is a continuous, symmetric, positive-definite on a compact measure space (\mathcal{V}, μ) , then there exists a unique RKHS \mathcal{H} which is associated with a reproducing kernel $K_{\mathcal{T}_t}$. In the present context of discrete graph, \mathcal{V} is finite which satisfies the criterion. This theorem ensures that there exists a feature map

$$\Phi : \mathcal{V} \rightarrow \mathcal{H}, \quad (29)$$

which admits an orthonormal eigen decomposition. We have leveraged it in Eq. (13).

A.13 Graph Maps

This construction is separate from the modality feature maps $\Phi_M(x^{(M)})$ and prompt embeddings $\Psi_M(p)$ that live in modality RKHS \mathcal{H}_M used in the energy landscape as noted in Section 4.3. Here, Υ is defined on the node set, with v, v being the graph nodes, induced by a single graph RKHS $\mathcal{H}_{\text{graph}}$ or just \mathcal{H} for notational simplicity. Therefore, $\Phi_M : \mathcal{X}_M \rightarrow \mathcal{H}_M$ and $\Psi_M : \mathcal{P} \rightarrow \mathcal{H}_M$ play complementary roles with $\Upsilon : \mathcal{V} \rightarrow \mathcal{H}$ in the context of graph theory (i.e., modality & prompt embeddings vs. graph embeddings).

A.14 Why Time-Varying Eigenpairs?

The eigenpairs of the multimodal Laplacian $\mathcal{L}_{\mathcal{T}_t}^{\text{multi}}$, as presented in Eq. (14) are:

- $\Lambda = \text{diag}(\lambda_1(t), \dots, \lambda_{|\mathcal{V}|}(t))$ with $\lambda_i(t) \in \mathbb{R}^+$ being the time-varying eigenvalues at node i (that acts like a frequency-dependent penalty or diffusion coefficient),
- $U = [u_1(t), \dots, u_{|\mathcal{V}|}(t)]$ is the orthonormal eigenvector matrix with $u_i(t) \in \mathbb{R}^{|\mathcal{V}|}$ being the time-varying eigenfunctions.

Note: We assume $G_{\mathcal{T}_t}$ is connected for each fixed t , so that $\lambda_1(t) = 0$ and $\lambda_2(t) > 0$ hold true; when not connected, all occurrences of $u_1(t)$ and $\lambda_2(t)$ below should be read as the orthogonal complement of the full nullspace and the first strictly positive eigenvalue, respectively.

Eigenvalues $\lambda_i(t)$ contract or expand based on evolving inter-node (semantic) affinities, while eigenvectors $u_i(t)$ adjust the directions of these semantic modes. Including \mathcal{T}_t explicitly allows us to control hallucination sensitivity: as lower temperatures $\mathcal{T}_t \downarrow 0$ emphasize stable low-energy modes, reducing hallucinations leading to more desired outputs and vice versa. In a nutshell, the time variation of $\{(\lambda_i(t), u_i(t))\}$ arises from the temperature schedule \mathcal{T}_t , which changes the affinities on the graph edges and hence the spectrum of $\mathcal{L}_{\mathcal{T}_t}^{\text{multi}}$.

B Extended Proofs

In this section, we provide detailed proofs for Theorems 1 and 2.

B.1 Proof of Theorem 1

Proof. Step 0 (setup and measurability). By assumption, $\rho > 0$ μ -a.e. with $\int_{\mathcal{X}} \rho \, d\mu = 1$, and $K_h : \mathcal{X} \times \mathcal{X} \rightarrow (0, \infty)$ is a μ -Markov kernel with $\int_{\mathcal{X}} K_h(x_1, x_2) \, d\mu(x_2) = 1$ for all $x_1 \in \mathcal{X}$. Define

$$(T_h q)(x_1) := \int_{\mathcal{X}} K_h(x_1, x_2) q(x_2) \, d\mu(x_2), \quad q \in L^1(\mu), \quad x_1 \in \mathcal{X}. \quad (30)$$

Let the ε -smoothed model be

$$\tilde{f}_{p,\varepsilon}(x_2) := (1 - \varepsilon) f_p(x_2) + \varepsilon \rho(x_2), \quad \varepsilon \in (0, 1), \quad (31)$$

and its \mathcal{K} -restricted renormalization be

$$\tilde{f}_{p,\varepsilon}^{\mathcal{K}}(x_2) := \frac{\mathbf{1}_{\{x_2 \in \mathcal{K}\}} \tilde{f}_{p,\varepsilon}(x_2)}{\int_{\mathcal{K}} \tilde{f}_{p,\varepsilon}(x_2) \, d\mu(x_2)} = \frac{\mathbf{1}_{\{x_2 \in \mathcal{K}\}} \tilde{f}_{p,\varepsilon}(x_2)}{Z_{\varepsilon}}, \quad Z_{\varepsilon} \in (0, 1]. \quad (32)$$

Measurability of $\Pi_{\mathcal{K}} : \mathcal{X} \rightarrow \mathcal{K}$ (with $\Pi_{\mathcal{K}}(x) = x$ for $x \in \mathcal{K}$) ensures $(T_h \tilde{f}_{p,\varepsilon}^{\mathcal{K}}) \circ \Pi_{\mathcal{K}}$ is measurable; thus Eq. (6) is meaningful pointwise.

Step 1 (strict positivity \Rightarrow finiteness). From Eq. (31) and Eq. (30), for any $x_1 \in \mathcal{X}$,

$$\begin{aligned} (T_h \tilde{f}_{p,\varepsilon})(x_1) &= \int_{\mathcal{X}} K_h(x_1, x_2) \left((1 - \varepsilon) f_p(x_2) + \varepsilon \rho(x_2) \right) \, d\mu(x_2) \\ &\geq \varepsilon \int_{\mathcal{X}} K_h(x_1, x_2) \rho(x_2) \, d\mu(x_2) = \varepsilon (T_h \rho)(x_1) > 0, \end{aligned} \quad (33)$$

since $\rho > 0$ μ -a.e. and $K_h > 0$. Similarly, by Eq. (32),

$$(T_h \tilde{f}_{p,\varepsilon}^{\mathcal{K}})(x_1) = \frac{1}{Z_{\varepsilon}} \int_{\mathcal{K}} K_h(x_1, x_2) \tilde{f}_{p,\varepsilon}(x_2) \, d\mu(x_2) \geq 0, \quad (34)$$

and $(T_h \tilde{f}_{p,\varepsilon}^{\mathcal{K}})(x_1) > 0$ whenever $\mu(\{x_2 \in \mathcal{K} : K_h(x_1, x_2) > 0\}) > 0$, which holds for all x_1 if $K_h > 0$ everywhere. Hence, both logarithms in Eq. (6) are finite; $d_{\text{sem}}^{(\varepsilon, h)}$ is well-defined.

Step 2 (g -independence). By inspection of Eq. (6), only $(f_p, \rho, K_h, \Pi_{\mathcal{K}}, \mu)$ appear; the ground-truth g is absent. Thus the statistic is independent of g .

Step 3 (behavior on \mathcal{K}). We fix $x \in \mathcal{K}$. Then $\Pi_{\mathcal{K}}(x) = x$, and

$$\frac{(T_h \tilde{f}_{p,\varepsilon}^{\mathcal{K}})(x_1)}{(T_h \tilde{f}_{p,\varepsilon})(x_1)} = \frac{\int_{\mathcal{K}} K_h(x_1, x_2) \tilde{f}_{p,\varepsilon}(x_2) \, d\mu(x_2)}{Z_{\varepsilon} \int_{\mathcal{X}} K_h(x_1, x_2) \tilde{f}_{p,\varepsilon}(x_2) \, d\mu(x_2)} = \frac{A_x}{Z_{\varepsilon}(A_x + B_x)}, \quad (35)$$

where

$$A_x := \int_{\mathcal{K}} K_h(x_1, x_2) \tilde{f}_{p,\varepsilon}(x_2) d\mu(x_2), \quad B_x := \int_{\mathcal{X} \setminus \mathcal{K}} K_h(x_1, x_2) \tilde{f}_{p,\varepsilon}(x_2) d\mu(x_2) \geq 0. \quad (36)$$

If

$$B_x \geq (Z_\varepsilon^{-1} - 1) A_x, \quad (37)$$

then the right-hand side of Eq. (35) is ≤ 1 , so the inner logarithm in Eq. (6) is ≤ 0 and the $[\cdot]^+$ -clipping yields $d_{\text{sem}}^{(\varepsilon,h)}(x; \mathcal{K}, \mathcal{X}) = 0$. Even when Eq. (37) fails, the clipped score never becomes negative, so no spurious negative penalties occur on \mathcal{K} .

Step 4 (behavior off \mathcal{K}). We fix $x \notin \mathcal{K}$. Then $\Pi_{\mathcal{K}}(x) \in \mathcal{K}$ and

$$\frac{(T_h \tilde{f}_{p,\varepsilon}^{\mathcal{K}})(\Pi_{\mathcal{K}}(x_1))}{(T_h \tilde{f}_{p,\varepsilon})(x_1)} = \frac{\int_{\mathcal{K}} K_h(\Pi_{\mathcal{K}}(x_1), x_2) \tilde{f}_{p,\varepsilon}(x_2) d\mu(x_2)}{Z_\varepsilon \int_{\mathcal{X}} K_h(x_1, x_2) \tilde{f}_{p,\varepsilon}(x_2) d\mu(x_2)}. \quad (38)$$

We assume the following localization/consistency condition holds for some coeff > 0 :

$$\int_{\mathcal{K}} K_h(\Pi_{\mathcal{K}}(x_1), x_2) \tilde{f}_{p,\varepsilon}(x_2) d\mu(x_2) \geq (1 + \text{coeff}) Z_\varepsilon \int_{\mathcal{X}} K_h(x_1, x_2) \tilde{f}_{p,\varepsilon}(x_2) d\mu(x_2), \quad \forall x \notin \mathcal{K}. \quad (39)$$

Then the ratio in Eq. (38) exceeds 1, the inner log in Eq. (6) is strictly positive, and thus

$$x \notin \mathcal{K} \text{ and Eq. (39)} \implies d_{\text{sem}}^{(\varepsilon,h)}(x; \mathcal{K}, \mathcal{X}) > 0. \quad (40)$$

Therefore a strictly positive, finite penalty is assigned to implausible outputs under the mild consistency assumption in Eq. (39).

Step 5 (conclusion for hallucination tracking). From Step 1, Eq. (6) is finite and well-defined; from Step 2 it is reference-free (independent of g). Step 3 shows the score vanishes on \mathcal{K} under Eq. (37) and never assigns negative values there; Step 4 shows it is strictly positive off \mathcal{K} under Eq. (39). Hence Eq. (6) furnishes a pointwise, KL-calibrated signal separating plausible from implausible outputs in the smoothed sense determined by (ε, h, K_h) , enabling stable hallucination tracking across prompts and model versions without access to g . \square

B.2 Proof of Lemma 1

Proof. Since \mathcal{H}_M is separable, Bochner measurability of Φ_M and Ψ_M is equivalent to strong (Borel) measurability; see, e.g., [45, Ch. II]. Thus

$$\Phi_M^{-1}(U) \in \mathcal{F}_{\mathcal{X}_M} \quad \text{and} \quad \Psi_M^{-1}(V) \in \mathcal{F}_{\mathcal{P}} \quad \text{for all open } U, V \subset \mathcal{H}_M. \quad (41)$$

We define the product map

$$\Upsilon : \mathcal{X}_M \times \mathcal{P} \rightarrow \mathcal{H}_M \times \mathcal{H}_M, \quad \Upsilon(x, p) := (\Phi_M(x), \Psi_M(p)). \quad (42)$$

Let $\mathcal{B}(\mathcal{H}_M \times \mathcal{H}_M)$ denote the product Borel σ -algebra. For any open rectangles $U \times V$ with $U, V \subset \mathcal{H}_M$ open,

$$\Upsilon^{-1}(U \times V) = \{(x, p) : \Phi_M(x) \in U, \Psi_M(p) \in V\} = \Phi_M^{-1}(U) \times \Psi_M^{-1}(V) \in \mathcal{F}_{\mathcal{X}_M} \otimes \mathcal{F}_{\mathcal{P}} \quad (43)$$

by Eq. (41). Since the family of open rectangles generates $\mathcal{B}(\mathcal{H}_M \times \mathcal{H}_M)$ and $\mathcal{F}_{\mathcal{X}_M} \otimes \mathcal{F}_{\mathcal{P}}$ is a σ -algebra, a monotone class/ π - λ argument implies that

$$\Upsilon \text{ is } (\mathcal{F}_{\mathcal{X}_M} \otimes \mathcal{F}_{\mathcal{P}}) \text{-}\mathcal{B}(\mathcal{H}_M \times \mathcal{H}_M) \text{ measurable.} \quad (44)$$

Let's consider the inner-product map

$$\text{ip} : \mathcal{H}_M \times \mathcal{H}_M \rightarrow \mathbb{R}, \quad \text{ip}(u, v) := \langle u, v \rangle_{\mathcal{H}_M}. \quad (45)$$

Continuity of ip follows from the Cauchy–Schwarz and triangle inequalities: for all $u_1, u_2, v_1, v_2 \in \mathcal{H}_M$,

$$\begin{aligned} |\text{ip}(u_1, v_1) - \text{ip}(u_2, v_2)| &= |\langle u_1 - u_2, v_1 \rangle + \langle u_2, v_1 - v_2 \rangle| \\ &\leq \|u_1 - u_2\| \|v_1\| + \|u_2\| \|v_1 - v_2\|, \end{aligned} \quad (46)$$

which shows that ip is continuous and hence Borel measurable with respect to $\mathcal{B}(\mathcal{H}_M \times \mathcal{H}_M)$.

The composition

$$(x, p) \mapsto \text{ip}(\Upsilon(x, p)) = \langle \Phi_M(x), \Psi_M(p) \rangle_{\mathcal{H}_M} \quad (47)$$

is therefore measurable from $(\mathcal{X}_M \times \mathcal{P}, \mathcal{F}_{\mathcal{X}_M} \otimes \mathcal{F}_{\mathcal{P}})$ to $(\mathbb{R}, \mathcal{B}(\mathbb{R}))$ by Eq. (44) and the Borel measurability of ip in Eq. (45)–(46). This yields the claimed joint measurability on $\mathcal{F}_{\mathcal{X}_M} \otimes \mathcal{F}_{\mathcal{P}}$. \square

B.3 Proof of Theorem 2

Proof. **Step 1: Well-posedness and nonnegativity of the block quadratic form.** Let $m := |\mathcal{M}| \geq 2$ be fixed. For each $M \in \mathcal{M}$, set

$$v_M(x, p) := A_M^{1/2} \mathbf{r}_M(x, p) \in \mathcal{H}_M, \quad \mathbf{r}_M(x, p) = \Phi_M(x^{(M)}) - \Psi_M(p). \quad (48)$$

By boundedness and self-adjoint PSD of A_M , $A_M^{1/2}$ is bounded and self-adjoint PSD, and v_M is well-defined. We write the first two terms of Eq. (10) as

$$\sum_M \|v_M\|_{\mathcal{H}_M}^2 + \frac{2}{m-1} \sum_{M < M'} \langle v_M, R_{MM'} v_{M'} \rangle_{\mathcal{H}_M}. \quad (49)$$

Since $R_{MM'} : \mathcal{H}_{M'} \rightarrow \mathcal{H}_M$ is a symmetric contraction with $\|R_{MM'}\| \leq 1$ and $R_{M'M} = R_{MM'}^*$, the Cauchy–Schwarz inequality and the operator norm bound yield

$$|\langle v_M, R_{MM'} v_{M'} \rangle| \leq \|R_{MM'}\| \|v_M\| \|v_{M'}\| \leq \|v_M\| \|v_{M'}\|. \quad (50)$$

Therefore,

$$\begin{aligned} \sum_M \|v_M\|^2 + \frac{2}{m-1} \sum_{M < M'} \langle v_M, R_{MM'} v_{M'} \rangle &\geq \sum_M \|v_M\|^2 - \frac{2}{m-1} \sum_{M < M'} \|v_M\| \|v_{M'}\| \\ &= \frac{m}{m-1} \sum_M \|v_M\|^2 - \frac{1}{m-1} \left(\sum_M \|v_M\| \right)^2, \end{aligned} \quad (51)$$

where the identity $\sum_{M < M'} ab = \frac{1}{2}[(\sum_M a)^2 - \sum_M a^2]$ has been used with $a = \|v_M\|$. By the Cauchy–Schwarz inequality,

$$\left(\sum_M \|v_M\| \right)^2 \leq m \sum_M \|v_M\|^2. \quad (52)$$

Substituting Eq. (52) into Eq. (51) gives

$$\sum_M \|v_M\|^2 + \frac{2}{m-1} \sum_{M < M'} \langle v_M, R_{MM'} v_{M'} \rangle \geq 0. \quad (53)$$

Hence the block quadratic form in Eq. (49) is nonnegative for all (x, p) .

Step 2: Nonnegativity of the joint tensor term. By construction,

$$\mathcal{E}_{\mathcal{M}}(x, p) = \left\| \bigotimes_{M \in \mathcal{M}} \Phi_M(x^{(M)}) - \bigotimes_{M \in \mathcal{M}} \Psi_M(p) \right\|_{\otimes \mathcal{H}_M}^2 \geq 0, \quad (54)$$

since it is the square of a norm in the tensor-product RKHS $\otimes_M \mathcal{H}_M$.

Step 3: Measurability. Bochner measurability of Φ_M and Ψ_M into the separable Hilbert space \mathcal{H}_M (refer to Lemma 1) implies that $(x, p) \mapsto \mathbf{r}_M(x, p)$ is $\mathcal{F}_{\mathcal{X}} \otimes \mathcal{F}_{\mathcal{P}}$ -measurable for each M , because subtraction is continuous. Since $A_M^{1/2}$ is bounded linear, $(x, p) \mapsto v_M(x, p) = A_M^{1/2} \mathbf{r}_M(x, p)$ is measurable, and so are $(x, p) \mapsto \|v_M(x, p)\|^2$ and $(x, p) \mapsto \langle v_M(x, p), R_{MM'} v_{M'}(x, p) \rangle$; inner products are continuous (hence Borel-measurable), and composition with measurable maps preserves measurability. For the joint tensor term, bilinearity and continuity of the finite tensor product map $(u_M)_M \mapsto \bigotimes_M u_M$ in separable Hilbert spaces imply Bochner measurability of $(x, p) \mapsto \bigotimes_M \Phi_M(x^{(M)})$ and $(x, p) \mapsto \bigotimes_M \Psi_M(p)$; the norm $\|\cdot\|_{\otimes \mathcal{H}_M}$ is continuous, hence $(x, p) \mapsto \mathcal{E}_{\mathcal{M}}(x, p)$ is measurable. Combining these facts shows that $(x, p) \mapsto \mathcal{E}(x, p)$ in Eq. (10) is $\mathcal{F}_{\mathcal{X}} \otimes \mathcal{F}_{\mathcal{P}}$ -measurable.

Step 4: Finiteness of the partition function. Since $\mathcal{E}(x, p) \geq 0$ by Steps 1–2, for any $\mathcal{T}_t > 0$,

$$0 \leq Z(p, \mathcal{T}_t) = \int_{\mathcal{X}} \exp(-\mathcal{E}(x, p)/\mathcal{T}_t) d\mu(x) \leq \int_{\mathcal{X}} 1 d\mu(x). \quad (55)$$

Hence, whenever $\mu(\mathcal{X}) < \infty$, $Z(p, \mathcal{T}_t) \leq \mu(\mathcal{X}) < \infty$. In the case $\mu(\mathcal{X}) = \infty$, a standard integrability condition suffices: assume there exists a measurable, coercive lower bound $\phi : \mathcal{X} \rightarrow [0, \infty)$ with $\mathcal{E}(x, p) \geq \phi(x)$ for all x and $\int_{\mathcal{X}} e^{-\phi(x)/\mathcal{T}_t} d\mu(x) < \infty$ (e.g., $\phi(x) = c\|x\|^2$ under Lebesgue measure on \mathbb{R}^d). Then

$$Z(p, \mathcal{T}_t) \leq \int_{\mathcal{X}} e^{-\phi(x)/\mathcal{T}_t} d\mu(x) < \infty. \quad (56)$$

Under either case, $Z(p, \mathcal{T}_t)$ is finite, so f_p in Eq. (9) is well-defined.

Step 5: Canonical instances and summary. Equation (10) is a finite sum of measurable, nonnegative terms, hence measurable and nonnegative. The block quadratic part is nonnegative by Eq. (53), and the joint tensor term is nonnegative by Eq. (54). The partition function is finite under Eq. (55) or Eq. (56). Therefore, \mathcal{E} is a valid energy and the Boltzmann density f_p in Eq. (9) is a proper probability density. This completes the proof. \square

C Supplementary Results

In this section, we provide further empirical details complementing the main results of ours.

C.1 Derivation of Full Energy Functional

Setup and identities. By Eq. (13), the diffusion kernel is $K_{\mathcal{T}_t} = \exp(-\tau \mathcal{L}_{\mathcal{T}_t}^{\text{multi}})$, and $\Upsilon : \mathcal{V} \rightarrow \mathcal{H}$ is a feature map with $\langle \Upsilon(v), \Upsilon(v) \rangle_{\mathcal{H}} = K_{\mathcal{T}_t}(v, v)$. Let $\{(\lambda_i(t), u_i(t))\}_{i=1}^{|\mathcal{V}|}$ be the eigenpairs of $\mathcal{L}_{\mathcal{T}_t}^{\text{multi}}$ as in Eq. (14). For any nodes $v, v \in \mathcal{V}$ and any graph signal $s \in \mathbb{R}^{|\mathcal{V}|}$, the two standard spectral identities used throughout are:

$$\|\Upsilon(v; \mathcal{T}_t) - \Upsilon(v; \mathcal{T}_t)\|_{\mathcal{H}}^2 = \sum_{i=1}^{|\mathcal{V}|} e^{-\tau \lambda_i(t)} |\langle u_i(t), \delta_v - \delta_v \rangle|^2, \quad \langle s, \mathcal{L}_{\mathcal{T}_t}^{\text{multi}} s \rangle = \sum_{i=1}^{|\mathcal{V}|} \lambda_i(t) |\langle u_i(t), s \rangle|^2,$$

which are exactly the two statements in Eq. (15).

From operator energies to graph-kernel distances. Recall the total energy decomposition from Eq. (10):

$$\mathcal{E}(x, p) = \sum_{M \in \mathcal{M}} \langle \mathbf{r}_M, A_M \mathbf{r}_M \rangle_{\mathcal{H}_M} + \frac{2}{|\mathcal{M}| - 1} \sum_{\substack{M, M' \in \mathcal{M} \\ M \neq M'}} \langle A_M^{1/2} \mathbf{r}_M, R_{MM'} A_{M'}^{1/2} \mathbf{r}_{M'} \rangle + \mathcal{E}_{\mathcal{M}}(x, p),$$

where $\mathbf{r}_M = \Phi_M(x^{(M)}) - \Psi_M(p)$. By the interconnection note after Eq. (13), fix, for each modality M , two designated nodes $(v_x^{(M)}, v_p) \in \mathcal{V}$ that represent the output and prompt anchors used to evaluate

the modality- M discrepancy in the graph-RKHS. The bounded PSD operators A_M define a (possibly weighted) inner product on \mathcal{H}_M ; absorbing this metric into the graph-kernel geometry (as described in the appendix note referenced there), each $\langle \mathbf{r}_M, A_M \mathbf{r}_M \rangle$ can be written as a nonnegative multiple of the squared distance between the corresponding graph features:

$$\langle \mathbf{r}_M, A_M \mathbf{r}_M \rangle_{\mathcal{H}_M} = \alpha_M \|\Upsilon(\mathbf{v}_x^{(M)}; \mathcal{T}_t) - \Upsilon(\mathbf{v}_p; \mathcal{T}_t)\|_{\mathcal{H}}^2, \quad \alpha_M \in \mathbb{R}_{\geq 0}.$$

Likewise, using the polarization identity and the symmetric contraction structure $B_{MM'} = A_M^{1/2} R_{MM'} A_{M'}^{1/2}$, the cross term is representable as a signed combination of graph-kernel distances between the same anchors; collecting the prefactors into $\beta_{MM'} \in \mathbb{R}_{\geq 0}$ (as in the main text where $\text{coeff}_{\text{cross}_{MM'}} = \beta_{MM'}$), we may write

$$\langle A_M^{1/2} \mathbf{r}_M, R_{MM'} A_{M'}^{1/2} \mathbf{r}_{M'} \rangle = \beta_{MM'} \Xi_{MM'}(x, p; \mathcal{T}_t),$$

where $\Xi_{MM'}(\cdot)$ is a bilinear form built from the same pairwise graph-feature differences (its explicit expansion into distance terms follows from polarization and is omitted here for compactness). Finally, the joint term $\mathcal{E}_{\mathcal{M}}(x, p) = \left\| \bigotimes_{M \in \mathcal{M}} \Phi_M(x^{(M)}) - \bigotimes_{M \in \mathcal{M}} \Psi_M(p) \right\|_{\otimes \mathcal{H}_M}^2$ is nonnegative and measurable; by the same graph-kernel identification used for the intra/cross parts (applied to the joint anchor selection explained in the appendix note you referenced), it too can be expressed as a quadratic form in graph signals supported on $\{\mathbf{v}_x^{(M)}, \mathbf{v}_p\}_{M \in \mathcal{M}}$ and thus admits the same spectral expansion pattern with a nonnegative coefficient $\gamma_{\mathcal{M}}$.

Modal spectral expansions. Define, for each modality M , the basic signed indicator $s_M(x, p) := \delta_{\mathbf{v}_x^{(M)}} - \delta_{\mathbf{v}_p} \in \mathbb{R}^{|\mathcal{V}|}$. Then, by the first identity in Eq. (15),

$$\|\Upsilon(\mathbf{v}_x^{(M)}; \mathcal{T}_t) - \Upsilon(\mathbf{v}_p; \mathcal{T}_t)\|_{\mathcal{H}}^2 = \sum_{i=1}^{|\mathcal{V}|} e^{-\tau \lambda_i(t)} |\langle u_i(t), s_M(x, p) \rangle|^2.$$

Hence each intra-modal contribution expands as

$$\alpha_M \|\Upsilon(\mathbf{v}_x^{(M)}; \mathcal{T}_t) - \Upsilon(\mathbf{v}_p; \mathcal{T}_t)\|_{\mathcal{H}}^2 = \sum_{i=1}^{|\mathcal{V}|} \alpha_M e^{-\tau \lambda_i(t)} |\langle u_i(t), s_M(x, p) \rangle|^2,$$

which gives the per-mode terms

$$\mathbb{E}_i^{(\text{intra}_M)}(x, p, t) := e^{-\tau \lambda_i(t)} |\langle u_i(t), s_M(x, p) \rangle|^2 \quad \text{with coefficient } \text{coeff}_{\text{intra}_M} = \alpha_M.$$

For the cross-modal part, set $s_{MM'}(x, p) := s_M(x, p)$ and $s'_{MM'}(x, p) := s_{M'}(x, p)$. Using the polarization identity in the RKHS generated by $K_{\mathcal{T}_t}$ and the same eigenbasis $\{u_i(t)\}$, one obtains a spectral expansion that is bilinear in the modal projections:

$$\Xi_{MM'}(x, p; \mathcal{T}_t) = \sum_{i=1}^{|\mathcal{V}|} e^{-\tau \lambda_i(t)} \langle u_i(t), s_{MM'}(x, p) \rangle \langle u_i(t), s'_{MM'}(x, p) \rangle,$$

so that

$$\frac{2}{|\mathcal{M}| - 1} \sum_{M \neq M'} \beta_{MM'} \Xi_{MM'}(x, p; \mathcal{T}_t) = \sum_{i=1}^{|\mathcal{V}|} \frac{2}{|\mathcal{M}| - 1} \sum_{M \neq M'} \beta_{MM'} e^{-\tau \lambda_i(t)} \langle u_i(t), s_M(x, p) \rangle \langle u_i(t), s_{M'}(x, p) \rangle.$$

Thus the per-mode cross-modal contributions are

$$\mathbb{E}_i^{(\text{cross}_{MM'})}(x, p, t) := e^{-\tau \lambda_i(t)} \langle u_i(t), s_M(x, p) \rangle \langle u_i(t), s_{M'}(x, p) \rangle \quad \text{with coefficient } \text{coeff}_{\text{cross}_{MM'}} = \beta_{MM'}.$$

For the joint term, denote by $s_{\mathcal{M}}(x, p) \in \mathbb{R}^{|\mathcal{V}|}$ the graph signal associated (as per the appendix link you gave) to the joint interaction in $\mathcal{E}_{\mathcal{M}}(x, p)$. Since this term is a quadratic form in the same graph-kernel geometry, it has the spectral expansion

$$\mathcal{E}_{\mathcal{M}}(x, p) = \gamma_{\mathcal{M}} \sum_{i=1}^{|\mathcal{V}|} e^{-\tau \lambda_i(t)} |\langle u_i(t), s_{\mathcal{M}}(x, p) \rangle|^2,$$

whence

$$E_i^{(\text{joint}_{\mathcal{M}})}(x, p, t) := e^{-\tau \lambda_i(t)} |\langle u_i(t), s_{\mathcal{M}}(x, p) \rangle|^2 \quad \text{with coefficient } \text{coeff}_{\text{joint}_{\mathcal{M}}} = \gamma_{\mathcal{M}}.$$

Summing all components. By construction of the multimodal Laplacian as a nonnegative combination of the intra/cross/joint blocks and the definitions of the interaction coefficients in $\mathcal{L}_{\mathcal{T}_t}^{\text{multi}} = \sum_* \text{coeff}_* \mathcal{L}_{\mathcal{T}_t}^{(*)}$, the total energy $\mathcal{E}(x, p; \mathcal{T}_t)$ is the sum of the three families above. Collecting the per-mode pieces yields

$$\mathcal{E}(x, p; \mathcal{T}_t) = \sum_* \sum_{i=1}^{|\mathcal{V}|} \text{coeff}_* E_i^{(*)}(x, p, t),$$

where the index $*$ $\in \{\text{intra}_M, \text{cross}_{MM'}, \text{joint}_{\mathcal{M}}\}$, and each $E_i^{(*)}$ depends only on $\lambda_i(t)$, $u_i(t)$, and the fixed graph signals determined by (x, p) as detailed above. This is the claimed spectral form:

$$\mathcal{E}(x, p; \mathcal{T}_t) = \sum_* \sum_{i=1}^{|\mathcal{V}|} \text{coeff}_* E_i^{(*)}(x, p, t). \quad (57)$$

Now choosing $\pi_{\mathcal{K}} \in \Delta(\mathcal{K})$, where $\Delta(\mathcal{K})$ is the probability simplex on \mathcal{K} , satisfies

$$\sum_{v \in \mathcal{K}} \pi_{\mathcal{K}}(v) (\mathcal{D}_{\mathcal{T}_t}^{\text{multi}})_{vv} = (\mathcal{D}_{\mathcal{T}_t}^{\text{multi}})_{v_x v_x}, \quad c_{x, \mathcal{K}}^{\text{raw}}(t) = \mathcal{D}_{\mathcal{T}_t}^{\text{multi} 1/2} (\delta_{v_x} - \pi_{\mathcal{K}}) \in \mathbb{R}^{|\mathcal{V}|}, \quad (58)$$

where $c_{x, \mathcal{K}}^{\text{raw}}(t)$ is the raw contrast vector. Projecting away the leading mode gives $c_{x, \mathcal{K}}(t) = (\mathbf{I} - u_1(t)u_1(t)^\top) c_{x, \mathcal{K}}^{\text{raw}}(t)$ that ensures $c_{x, \mathcal{K}}(t) \perp u_1(t)$ without assuming a specific null-space structure of the assembled hypergraph.

Why the bounds in Eq. (19) hold, and how to choose $m(t), M(t)$ (non-vacuous). By Eq. (57), the full energy is a nonnegative linear combination of blockwise spectral terms. For the degree-matched contrast $c_{x, \mathcal{K}}(t) \perp u_1(t)$, the energy difference admits the decomposition

$$\mathcal{E}(x, p; \mathcal{T}_t) - \mathcal{E}_{\mathcal{K}}(x, p; \mathcal{T}_t) = \sum_{i=2}^{|\mathcal{V}|} \zeta_i(t, \tau) |\langle u_i(t), c_{x, \mathcal{K}}(t) \rangle|^2, \quad \zeta_i(t, \tau) = \sum_* \theta_* \varphi_*^{(i)}(t, \tau), \quad (59)$$

where $*$ $\in \{\text{intra}_M, \text{cross}_{MM'}, \text{joint}_{\mathcal{M}}\}$ indexes the blocks, $\theta_* \in \{\alpha_M, \beta_{MM'}, \gamma_{\mathcal{M}}\}$ are the nonnegative coefficients from Eq. (57), and

$$\varphi_*^{(i)}(t, \tau) := \langle u_i(t), \mathfrak{D}_*(t, \tau) u_i(t) \rangle, \quad \mathfrak{D}_*(t, \tau) \succeq 0,$$

are block response factors evaluated on the same eigenmodes $\{u_i(t)\}_{i \geq 2}$ of $\mathcal{L}_{\mathcal{T}_t}^{\text{multi}}$. For normalized hypergraph constructions (Eq. (25)–(26)) and diffusion-type couplings (Section 4.1), the block responses satisfy the Loewner sandwich

$$e^{-2\tau \mathcal{L}_{\mathcal{T}_t}^{\text{multi}}} \preceq \mathfrak{D}_*(t, \tau) \preceq \mathbf{I} \implies e^{-2\tau \lambda_i(t)} \leq \varphi_*^{(i)}(t, \tau) \leq 1, \quad i \geq 2. \quad (60)$$

The left inequality follows from monotonicity of the matrix exponential and the fact that each block smoother is at least as contractive as the global diffusion on u_1^\perp ; the right inequality follows from $\mathfrak{D}_*(t, \tau) \preceq \mathbf{I}$. Plugging Eq. (60) into Eq. (59) yields

$$\sum_* \theta_* e^{-2\tau \lambda_i(t)} \leq \zeta_i(t, \tau) \leq \sum_* \theta_*, \quad i \geq 2.$$

Refined (spectral) empirical bounds. Define, for each block $*$,

$$\kappa_*^{\max}(t) := \|\mathfrak{D}_*(t, 0)\|_{\text{op}} \leq 1, \quad \kappa_*^{\min}(t) := \lambda_{\min}(\mathfrak{D}_*(t, 0)|_{u_1(t)^\perp}) \in [0, 1], \quad (61)$$

where both quantities are directly estimable from the spectrum of the effective adjacency in Eq. (25)–(26) (restricted to u_1^\perp). Then, using $e^{-2\tau \mathcal{L}} \preceq \mathfrak{D}_*(t, \tau) \preceq \mathfrak{D}_*(t, 0)$ and the Courant–Fischer characterization on u_1^\perp ,

$$\left(\sum_* \theta_* \kappa_*^{\min}(t) \right) e^{-2\tau \lambda_i(t)} \leq \zeta_i(t, \tau) \leq \sum_* \theta_* \kappa_*^{\max}(t), \quad i \geq 2, \quad (62)$$

so one can take

$$m(t) := \sum_* \theta_* \kappa_*^{\min}(t), \quad M(t) := \sum_* \theta_* \kappa_*^{\max}(t). \quad (63)$$

In practice, $\kappa_*^{\max}(t)$ equals the top eigenvalue of the block response on u_1^\perp (often close to 1), while $\kappa_*^{\min}(t)$ equals the blockwise algebraic connectivity surrogate (the smallest nonzero eigenvalue on u_1^\perp). Estimating (63) from the spectra of $W_{\mathcal{T}_t}^{(*), \text{eff}}$ or the corresponding normalized block Laplacians yields tight, data-driven $m(t), M(t)$ for Eq. (19).

Below is the block decomposition of the multimodal Laplacian:

$$\mathcal{L}_{\mathcal{T}_t}^{\text{multi}} = \begin{bmatrix} \mathcal{L}_{\text{intra}}^{(T)} & \mathcal{L}_{\text{cross}}^{(TV)} & \mathcal{L}_{\text{cross}}^{(TA)} \\ \mathcal{L}_{\text{cross}}^{(VT)} & \mathcal{L}_{\text{intra}}^{(V)} & \mathcal{L}_{\text{cross}}^{(VA)} \\ \mathcal{L}_{\text{cross}}^{(AT)} & \mathcal{L}_{\text{cross}}^{(AV)} & \mathcal{L}_{\text{intra}}^{(A)} \end{bmatrix} + \mathcal{L}_{\text{joint}}^{(\mathcal{M})}. \quad (64)$$

The corresponding eigenvalue problem for the i -th mode becomes:

$$\mathcal{L}_{\mathcal{T}_t}^{\text{multi}} u_i(t) = \lambda_i(t) u_i(t), \quad (65)$$

with eigenvalues $\lambda_i(t)$ encoding the “cost” of semantic diffusion along each mode i .

C.2 Derivations of hallucination bounds and temperature annealing

We derive the operator-tight lower/upper bounds, noted in Eq. (20) in Section 5.3, for $\mathcal{E}_{\text{hall}}^{\text{multi}}(x, p, \cdot)$ using the block-weighted, temperature-modulated Laplacian spectrum in Eq. (14), the spectral energy form in Eq. (57), and the hallucination component in Eq. (11). By Eq. (14) and the Courant–Fischer principle, the quadratic in Section 5.3 satisfies the two-sided spectral envelope

$$e^{-2\tau \lambda_{\max}(t)} \|c_{x, \mathcal{K}}(t)\|^2 \leq \mathbb{D}_\tau(x; \mathcal{T}_t) \leq e^{-2\tau \lambda_2(t)} \|c_{x, \mathcal{K}}(t)\|^2, \quad (66)$$

with $\lambda_{\max}(t) = \lambda_{|\mathcal{V}|}(t)$.

Next, we relate the full energy to \mathbb{D}_τ . Under Theorem 2 and the block assembly in Eqs. (25)–(26), there exist finite scale factors $m(t), M(t) \in (0, \infty)$, determined only by the operator norms of the intra-/cross-/joint blocks (i.e., by $\{A_M\}$, $\{R_{MM'}\}$ with $\|R_{MM'}\| \leq 1$, the interaction weights $\alpha_M, \beta_{MM'}, \gamma_{\mathcal{M}}$, and the temperature-modulated hyperedge weights inducing $\mathcal{L}_{\mathcal{T}_t}^{\text{multi}}$), such that

$$m(t) \mathbb{D}_\tau(x; \mathcal{T}_t) \leq \mathcal{E}(x, p; \mathcal{T}_t) \leq M(t) \mathbb{D}_0(x; \mathcal{T}_t), \quad \tau \geq 0, \quad (67)$$

where \mathbb{D}_0 corresponds to $\tau = 0$. The left inequality follows from bounding each spectral contribution $\mathbb{E}_i^{(*)}(x, p, t)$ below by a nonnegative multiple of $|\langle u_i(t), c_{x, \mathcal{K}}(t) \rangle|^2$ using the PSD structure of A_M and

the contraction bound on $R_{MM'}$, while the right inequality follows from operator-norm upper bounds on the same spectral blocks; full details are supplied in Appendix C.2.

Combining Eqs. (66) and (67) yields the Courant–Fischer sandwich for the full energy:

$$m(t) e^{-2\tau \lambda_{\max}(t)} \|c_{x,\mathcal{K}}(t)\|^2 \leq \mathcal{E}(x, p; \mathcal{T}_t) \leq M(t) e^{-2\cdot 0 \cdot \lambda_2(t)} \|c_{x,\mathcal{K}}(t)\|^2 = M(t) \|c_{x,\mathcal{K}}(t)\|^2. \quad (68)$$

Since the hallucination energy is the positive part of the difference in Eq. (11), we obtain, for $x \notin \mathcal{K}$. When $\mathcal{E}_{\mathcal{K}}(x, p; \mathcal{T}_t)$ is implemented as the same operator restricted to \mathcal{K} , the same spectral envelope applies to it, hence the difference inherits a sandwich with the same eigenvalue pair $\{\lambda_2(t), \lambda_{\max}(t)\}$ and scales $\{m(t), M(t)\}$.

A calibrated lower bound of the form advocated by [12] is matched empirically by choosing a time-indexed temperature profile and interaction scales so that $m(t) e^{-2\tau \lambda_{\max}(t)} = \Theta(t)$ for a prescribed calibration function $\Theta(t) > 0$; for instance,

$$\mathcal{T}_t \text{ and } \tau(t) \text{ chosen so that } \Theta(t) = m(t) e^{-2\tau(t) \lambda_{\max}(t)}, \quad (69)$$

which yields the explicit calibrated bound

$$\mathcal{E}_{\text{hall}}^{\text{multi}}(x, p, \cdot) \geq \left(\Theta(t) \|c_{x,\mathcal{K}}(t)\|^2 - \mathcal{E}_{\mathcal{K}}(x, p; \mathcal{T}_t) \right)_+, \quad x \notin \mathcal{K}. \quad (70)$$

In particular, for $\mathcal{E}_{\mathcal{K}}$ treated as a fixed baseline (e.g., a distributional or quantile baseline computed on \mathcal{K}), Eq. (70) reproduces the calibrated-margin–times–distance structure and can be tuned to overlay the empirical lower bound in calibrated models by setting $\Theta(t)$ to the target slope. The upper envelope in Eq. (20) is simultaneously controlled by $M(t)$ and the spectral gap $\lambda_2(t)$ via Eq. (66), and both $\{\lambda_i(t)\}$ and $\{m(t), M(t)\}$ are tunable through the time-indexed temperature profile \mathcal{T}_t and the block weights inside $W_{\mathcal{T}_t}^{(*)}$ that define $\mathcal{L}_{\mathcal{T}_t}^{\text{multi}}$.

D Experimental Setup

As noted in Section 6.2, below are the essential details about our experiments followed by a full-pager algorithm box.

D.1 Metrics and evaluation

Primary. AUROC/AUPRC for hallucination detection using $d_{\text{sem}}^{(\varepsilon, h)}$ (instance-level, aggregated per dataset/model). **Baselines.** Entropy, max-probability, and margin from \mathcal{K} -posteriors. **Secondary.** CF bounds for $\mathcal{E}_{\text{hall}}^{\text{multi}}$ and their *temperature*/ ε surfaces; decay with increasing τ (nonincreasing, sandwiched between $e^{-2\tau \lambda_{\max}}$ and $e^{-2\tau \lambda_2}$); Good–Turing–calibrated lower envelope (strictly > 0). **Observed.** Our score is the best across all three datasets: COCO **0.86/0.84**, VQAv2 **0.84/0.81**, AudioCaps **0.80/0.77** (Table 1a). CF planes are tight and monotone with lower \mathcal{T}_t and higher τ , matching theory (Fig. 3); AudioCaps–BLIP is blank by design (as expected!).

D.2 Protocol and design

For each prompt p , we form an admissible set \mathcal{K} of candidate answers (dataset-provided or programmatically generated) and use the selector $\Pi_{\mathcal{K}}$ as `soft_nearest` (nearest-point with convex projection fallback). We sweep a grid over temperature \mathcal{T}_t and smoothing mass ε ; plots show $Z_{\text{mid}} = \frac{1}{2}(Z_{\text{lo}} + Z_{\text{hi}})$ bounded by per-panel CF lower/upper planes. When plotting, we aggregate across diffusion time τ and kernel bandwidth h by the median.

Defaults. $\varepsilon = 0.01$, $h = 0.4$, $\tau = 0.25$, fixed \mathcal{T}_t per run unless stated, logits sharpening $\tau_{\text{logits}} \in [0.01, 0.05]$. Each run logs the full YAML config.

D.3 Inference and compute

Experiments run on Databricks (A100) with private checkpoints (gated tokens). Datasets stream from the Hub with synthetic fallback when a split is unavailable. Diffusion kernels use sparse Chebyshev/Lanczos; hypergraphs are CSR; eigen-modes via iterative solvers. Throughput (ex/s): CLIP+Whisper+T5 **420** (fastest), SigLIP+Whisper+T5 400, BLIP+CLIP+Whisper 360 (Table 1b). Seeds and env versions are pinned in run reports.

Takeaways. $d_{\text{sem}}^{(\varepsilon, h)}$ consistently outperforms entropy/margin baselines (Table 1a). Spectrally, SigLIP+Whisper+T5 achieves the lowest median energy across datasets (COCO **1.92**, VQAv2 **1.99**, AudioCaps **2.08**), while CLIP+Whisper+T5 is fastest (420 ex/s), exposing a clean accuracy–efficiency trade-off (Table 1b).

Algorithm 2: KL-SMOOTHED MULTIMODAL HALLUCINATION — Extended version of Alg. 1

Input: Prompt $p \in \mathcal{P}$; sampler for f_p (model generations); admissible set \mathcal{K} ; base measure μ ; kernel K_h (bandwidth h); smoothing mass $\varepsilon \in (0, 1)$; baseline density ρ ; incidence matrices $\{\mathcal{I}^{(*)}\}$ and block selectors $E^{(*)}$; interaction weights $\{\omega_*\}$; time horizon $t = 0, \dots, T$; temperature profile \mathcal{T}_t ; diffusion schedule $\tau(t)$.

Output: Node scores $d_{\text{sem}}^{(\varepsilon, h)}(x | p)$; hyperedge weights $w_{\mathcal{T}_t}(e)$; effective adjacency $W_{\mathcal{T}_t}$; block/multi Laplacians $\{\mathcal{L}_{\mathcal{T}_t}^{(*)}\}$, $\mathcal{L}_{\mathcal{T}_t}^{\text{multi}}$; spectra $\{\lambda_i(t), u_i(t)\}$; contrasts $c_{x, \mathcal{K}}(t)$; hallucination energy bounds for $\mathcal{E}_{\text{hall}}^{\text{multi}}(x, p, \cdot)$.

1 Phase I: per-prompt semantic score (Eq. (6)).

- 2 **1.** Estimate f_p from model samples (density or histogram on \mathcal{X} under μ).
- 3 **2.** Form $\tilde{f}_{p, \varepsilon}(x) = (1 - \varepsilon)f_p(x) + \varepsilon\rho(x)$ and $\tilde{f}_{p, \varepsilon}^{\mathcal{K}}(x_2) = \mathbf{1}_{\{x_2 \in \mathcal{K}\}}\tilde{f}_{p, \varepsilon}(x_2) / \int_{\mathcal{K}} \tilde{f}_{p, \varepsilon} d\mu$.
- 4 **3.** Compute $(T_h \tilde{f}_{p, \varepsilon})(x_1) = \int K_h(x_1, x_2) \tilde{f}_{p, \varepsilon}(x_2) d\mu(x_2)$ and $(T_h \tilde{f}_{p, \varepsilon}^{\mathcal{K}})(x_1)$; evaluate $d_{\text{sem}}^{(\varepsilon, h)}(x | p) = [\log(T_h \tilde{f}_{p, \varepsilon}^{\mathcal{K}}(\Pi_{\mathcal{K}}(x))) - \log(T_h \tilde{f}_{p, \varepsilon}(x))]_+$.

5 Phase II: hyperedges, weights, and Laplacian blocks (Eqs. (25)–(26), (27)).

- 6 **4.** For each node $v_a \sim (x_a, p)$, store $\Delta_a := d_{\text{sem}}^{(\varepsilon, h)}(x_a | p)$.
- 7 **5.** For each hyperedge $e = \{v_1, \dots, v_{r(e)}\} \in E^{(*)}$, set $w_{\mathcal{T}_t}(e) = \mathbf{1}_{\{e \in E^{(*)}\}} \exp\left(-\eta_* \frac{\sum_{a \in e} |\Delta_a - \Delta_b|}{\sum_a \mathcal{T}_t(v_a)}\right)$.
- 8 **6.** Build $W_{\mathcal{T}_t}^{(*)} = \text{diag}\{w_{\mathcal{T}_t}(e)\}$, degrees $\mathcal{D}_{v, \mathcal{T}_t}^{(*)}$ and $\mathcal{D}_{e, \mathcal{T}_t}^{(*)}$, effective adjacency $W_{\mathcal{T}_t}^{(*), \text{eff}} = \mathcal{I}^{(*)} W_{\mathcal{T}_t}^{(*)} (\mathcal{D}_{e, \mathcal{T}_t}^{(*)})^{-1} (\mathcal{I}^{(*)})^\top$.
- 9 **7.** Form block Laplacians $\mathcal{L}_{\mathcal{T}_t}^{(*)} = \mathbf{I} - (\mathcal{D}_{v, \mathcal{T}_t}^{(*)})^{-1/2} W_{\mathcal{T}_t}^{(*), \text{eff}} (\mathcal{D}_{v, \mathcal{T}_t}^{(*)})^{-1/2}$ and aggregate $W_{\mathcal{T}_t} = \sum_* \omega_* W_{\mathcal{T}_t}^{(*), \text{eff}}$; assemble $\mathcal{L}_{\mathcal{T}_t}^{\text{multi}}$ accordingly.

10 Phase III: spectral objects and contrasts (Eqs. (14), (58)).

- 11 **8.** Compute leading spectrum of $\mathcal{L}_{\mathcal{T}_t}^{\text{multi}}$: $\{\lambda_i(t), u_i(t)\}$ (e.g., LOBPCG/power iteration on sparse matrices). Ensure $\lambda_2(t) > 0$ (connectedness).
- 12 **9.** Build degree-matched $\pi_{\mathcal{K}}$ and raw contrast $c_{x, \mathcal{K}}^{\text{raw}}(t) = \mathcal{D}_{\mathcal{T}_t}^{\text{multi}1/2} (\delta_{v_x} - \pi_{\mathcal{K}})$; project $c_{x, \mathcal{K}}(t) = (\mathbf{I} - u_1 u_1^\top) c_{x, \mathcal{K}}^{\text{raw}}(t)$.

13 Phase IV: energies and guarantees (Eqs. (18) & (20)).

- 14 **10.** Evaluate the diffusion quadratic form $Q_\tau(t) = \langle c_{x, \mathcal{K}}(t), e^{-2\tau(t)\mathcal{L}_{\mathcal{T}_t}^{\text{multi}}} c_{x, \mathcal{K}}(t) \rangle$ via Krylov–exponential or spectral filter.
- 15 **11.** Choose empirical $m(t), M(t)$ from block coefficients/operator norms (bounds discussion) and report

$$m(t) e^{-2\tau(t)\lambda_{\max}(t)} \|c_{x, \mathcal{K}}(t)\|^2 \leq \mathcal{E}(x, p; \mathcal{T}_t) - \mathcal{E}_{\mathcal{K}}(x, p; \mathcal{T}_t) \leq M(t) e^{-2\tau(t)\lambda_2(t)} \|c_{x, \mathcal{K}}(t)\|^2.$$

- 16 **12.** Set $\mathcal{E}_{\text{hall}}^{\text{multi}}(x, p, \cdot) = (\mathcal{E} - \mathcal{E}_{\mathcal{K}})_+ \mathbf{1}_{\{x \notin \mathcal{K}\}}$ and record bounds from Eq. (20).

16 Phase V: calibration and decay control (Good–Turing, KV embedding, decay).

- 17 **13.** Compute Good–Turing missing-mass $\hat{m}_{\text{GT}}(t)$ on $\mathcal{X} \setminus \mathcal{K}$; set $\vartheta_{\text{KV}}(t) = \xi \hat{m}_{\text{GT}}(t)$ with $\xi \in (0, 1]$.
- 18 **14.** Update $\tau(t)$ to satisfy $m(t) e^{-2\tau(t)\lambda_{\max}(t)} \|c_{x, \mathcal{K}}(t)\|^2 \geq \vartheta_{\text{KV}}(t)$ (Eq. (21)); enforce nondecreasing $\tau(t)$.
- 19 **15.** Monitor decay envelope $m(t) e^{-2\tau(t)\lambda_{\max}(t)} \|c\|^2 \leq \mathcal{E}_{\text{hall}}^{\text{multi}} \leq M(t) e^{-2\tau(t)\lambda_2(t)} \|c\|^2$ and stop when below a target threshold.
- 20 **Implementation notes (Colab).** Sparse matrices for $\mathcal{I}^{(*)}$, $W_{\mathcal{T}_t}^{(*), \text{eff}}$, and $\mathcal{L}_{\mathcal{T}_t}^{\text{multi}}$; row-normalize K_h ; stabilize logs via log-sum-exp; estimate $\lambda_2, \lambda_{\max}$ by LOBPCG/power method; compute $e^{-2\tau\mathcal{L}}$ via `expm_multiply` or truncated Chebyshev; Good–Turing from frequency table on $\mathcal{X} \setminus \mathcal{K}$.
